

University of Alberta

Fast Photoresponse of Functionalized Pentacene Organic Molecular Crystals

by

Jianbo Gao



A thesis submitted to the Faculty of Graduate Studies and Research in partial fulfillment of
the requirements for the degree of *Master of Science*

Department of *Physics*

Edmonton, Alberta
Fall, 2004



Library and
Archives Canada

Bibliothèque et
Archives Canada

Published Heritage
Branch

Direction du
Patrimoine de l'édition

395 Wellington Street
Ottawa ON K1A 0N4
Canada

395, rue Wellington
Ottawa ON K1A 0N4
Canada

Your file *Votre référence*

ISBN: 0-612-95748-9

Our file *Notre référence*

ISBN: 0-612-95748-9

The author has granted a non-exclusive license allowing the Library and Archives Canada to reproduce, loan, distribute or sell copies of this thesis in microform, paper or electronic formats.

L'auteur a accordé une licence non exclusive permettant à la Bibliothèque et Archives Canada de reproduire, prêter, distribuer ou vendre des copies de cette thèse sous la forme de microfiche/film, de reproduction sur papier ou sur format électronique.

The author retains ownership of the copyright in this thesis. Neither the thesis nor substantial extracts from it may be printed or otherwise reproduced without the author's permission.

L'auteur conserve la propriété du droit d'auteur qui protège cette thèse. Ni la thèse ni des extraits substantiels de celle-ci ne doivent être imprimés ou autrement reproduits sans son autorisation.

In compliance with the Canadian Privacy Act some supporting forms may have been removed from this thesis.

Conformément à la loi canadienne sur la protection de la vie privée, quelques formulaires secondaires ont été enlevés de cette thèse.

While these forms may be included in the document page count, their removal does not represent any loss of content from the thesis.

Bien que ces formulaires aient inclus dans la pagination, il n'y aura aucun contenu manquant.

Canada

Acknowledgements

Special thanks to Dr. Frank A. Hegmann, my supervisor, who leads me into the door of scientific research, gives me support, encouragement, advice and especially, takes me as a family member in his group. I have benefit in many ways from his wise and humorous counsel. Special thanks also to the other professors of my supervisor committee, Dr. John Beamish and Dr. Rik R. Tykwinski for their insightful feedback and suggestion to revision of my thesis. I especially appreciate Dr. Tykwinski's help for providing me the crystals and teaching me how to make pentacene film and crystals. And finally, special thanks to Dr. Oksana Ostroverkhova, who always gave me the help I needed.

Thanks to other friends and colleagues for their help and advice: Dr. Kris Lui and Ting Weiyuan, who proofread various drafts of this work; Don Mullin, Greg Popowich and Tony Walford, who help me figure out the experimental problems.

I especially want to acknowledge my friends and colleagues who contribute to the completion of this thesis. Aaron Slepko, David Cooke, Grey Arnup. Although I am far away from my homeland, I never found myself far from a kind word or warm shoulder. To these people, I give my heartfelt thanks.

My greatest appreciation goes to Dan Cui, my wife, whose faith in my work often makes the difference.

The funding was provided by NSERC, CFI, iCORE, and ONR.

Table of Contents

Chapter 1 Introduction	1
1.1 Organic molecular crystals (Polyacenes)	1
1.2 The optical properties of organic molecular crystals	3
1.3 Functionalized pentacene chemical structure	5
1.4 Techniques for measuring transient photoconductivity	7
1.4.1 The time domain pump-probe technique	7
1.4.2 The time-of-flight technique	9
1.4.3 The Auston switch technique	11
Chapter 2 Charge Carrier Photogeneration and Transport Mechanisms in Organic Molecular Crystals	13
2.1 Charge carrier photogeneration mechanisms	14
2.1.1 Molecular exciton model	14
2.1.2 Electric field dependence according to the Onsager model	15
2.2 Charge carrier transport	18
2.2.1 Charge carrier transport mechanisms	18
2.2.2 Electrical field dependence	21
2.3 The impact of traps	23
2.4 Metal-semiconductor junctions –The Schottky barrier	23
Chapter 3 Sample Preparation and Experimental Setup	27
3.1 Sample preparation	27
3.1.1 Shadow mask and gold bulk cleaning	27
3.1.2 Pumping procedure for diffusion pump system	28
3.1.3 Sample mounting	30
3.2 Electrical components bandwidth test	31
3.3 Experimental setup	33
3.4 Noise reduction	35
3.5 Laser beam profile	37
Chapter 4 Results and Discussion	42
4.1 Typical fast photoresponse wave forms	42
4.2 Charge carrier transport and photogeneration in TIPS at room temperature	43
4.3 Charge carrier mobility comparison between SCLC and fast photoresponse experiments	46
4.4 Wave form comparison between full illumination and narrow focus	50
4.5 Electric field and laser fluence dependence	51
4.6 Built-in field at interface	54
Chapter 5 Conclusion and future work	58
Appendix	60
References	79

Lists of tables

Table 1.1

Characteristic features comparison between organic molecular and inorganic covalent crystals.

Table 4.1

Several sample dimensions and the corresponding fast photoresponse rise times.

Table A (1)

Crystallographic data of polyacenes.

Table A (2)

Ionization potentials, electron affinities and predicted band gaps of the polyacenes.

Table C (1)

Boundary conditions of the original potential planes and the conformed transformation planes.

Lists of figures

Figure 1.1

Chemical structures of polyacenes including naphthalene, anthracene, tetracene and pentacene.

Figure 1.2

The high resolution microscopy of copper hexadecachlorophthalocyanine molecule along the $a-b$ plane in the crystal. The picture presents that the individual molecules are separated by channels with negligible electron density due to the weak Van der Waals interaction.

Figure 1.3

Schematic electronic transition process in diatomic molecule, which occurs photons absorption and emission. The Franck-Condon principle states that the nuclei do not move during the optical transition. r_1 and r_2 are the equilibrium separations of the nuclei in the ground and excited state respectively. One of the atoms has a larger radius in the excited molecule because the atom itself is in an excited state.

Figure 1.4

Absorption and emission spectra of anthracene in solution.

Figure 1.5

The well known parent pentacene herring-bone structure.

Figure 1.6

TIPS single molecule chemical structure. R presents side group which enhances face-to-face interaction.

Figure 1.7

TIPS crystal chemical structure. View along the crystallographic b -axis, corresponding to the o -stacking axis, showing two-dimensional stacks of TIPS molecules together with space filling views of the crystal packing.

Figure 1.8

TIPS two-dimensional brick structure in the $a-b$ plane. (side groups are not shown).

Figure 1.9

Schematic setup of the time domain pump-probe technique. A probe beam and pump beam are split from a single ultrafast laser source.

Figure 1.10

Schematic setup of the time-of-flight experiment. It is sandwich geometry where electric field is across the electrode. The pulse laser shines one side to produce charge carriers which drift to generate photocurrent. The photocurrent signal is obtained by fast sampling oscilloscope through the amplifier.

Figure 1.11

- a) Ideal TOF current wave form without dispersion.
- b) Wave form with charge carrier dispersion. The sharp tail in the ideal case becomes longer and the shoulder indicates the transit time.
- c) Log-log scale of wave form b to get the transit time t_t indicated by the dashed line.

Figure 1.12

Schematic setup of the Auston switch technique. Thin Au or Al microstrip line was evaporated onto sample surface, which reduces capacitance. One side of the electrode is biased with electric field and the other side is connected to the fast sampling oscilloscope to get signal.

Figure 2.1

Multi-step photogeneration model in organic molecular crystal. 1st step, photon absorption and a neutral Frenkel exciton state formation; 2nd step, autoionization of the excited molecular state; 3rd step, formation of an intermediate charge pair state; 4th step, dissociation of the charge pair state.

S_1, S_2, S_3 : excited electronic states; K_f : rate constant of radiative intramolecular relaxation; K_{AI} : rate constant of direct autoionization; E_G^{Ad} : adiabatic energy gap; E_{CP} : energy of charge pair; U_{CP} : Columbic binding energy of charge pair; Ω : dissociation probability of charge pair state; r_{th} : mean thermalization length of hot charge carriers; M_p^+, M_p^- : molecular polaron states.

Figure 2.2

Spectral response of D.C. hole and electron photocurrents in anthracene at temperature of 179 K. Applied voltages: 300 V D.C.; specimen thickness: 0.5mm; light intensity: 6×10^{12} photons/sec. The arbitrary photocurrent units are the same for both hole and electron curves.

Figure 2.3

Spectral dependence of photocurrent quantum efficiency in anthracene single crystals.

Figure 2.4

The temperature dependence of the electron mobility along the c' direction in naphthalene single crystals. The first part curve can be fitted into $\mu \propto T^{-n}$ ($n = 1.7$), which follows band transport model.

Figure 2.5

Electrons and holes mobilities along a direction in ultrapure naphthalene vs temperature. The solid line indicates a T^{-n} power-law temperature dependence with exponents n as indicated in the figure. $\mu^- \propto T^{-1.4}$ for electrons and $\mu^+ \propto T^{-2.9}$ for holes.

Figure 2.6

Field-effect mobility dependence on temperature for three different pentacene thin film transistors, which were made under the same conditions. Curve (a) was fitted to the formula $\mu \propto \exp(-E_a / KT)$ and $E_a = 38 \text{ meV}$. It clearly shows that curve (c) is independent of temperature.

Figure 2.7

Hole drift velocity dependence on electric field in the a -direction of naphthalene crystal. It consists of linear, sub-linear and saturation region. The increasing electric field results in the charge carrier faster approach to the scattering sites, further increasing electrical field results in the onset of dominant scattering on optical phonons.

Figure 2.8 (a)

Band diagram of isolated metal and semiconductor. The Fermi level of metal is higher than the N-type semiconductor Fermi level.

E_F^m : Metal Fermi level; E_V : Semiconductor valence band; E_C : Semiconductor conduction band

ϕ_m : Metal work function; χ_S : Semiconductor work function; ϕ_S : Work function difference

Figure 2.8 (b)

Band diagram of isolated metal and semiconductor which are electrically connected.

δ : Separation between metal and semiconductor; W : Depletion layer; V_t : Electrostatic potential difference between metal and semiconductor

Figure 2.8 (c)

Band diagram of isolated metal and semiconductor which are separated by a narrow gap.

Figure 2.8 (d)

Band diagram of isolated metal and semiconductor which are in perfect contact.

Figure 3.1

Schematic setup of evaporation system. V1: Vent Valve; V2: Gate Valve ; V3: Roughing Valve; V4: Foreline Valve (Backing valve); G1: Penning Gauge ; G2: Thermotron Gauge.

Figure 3.2

Picture of the sample, PC board sample holder and SMA connector. The sample is pasted on the PC board slit using Epoxy paste. The copper on the PC board is soldered with the SMA electrodes.

Figure 3.3

Experimental setup for testing the bias tee bandwidth. Signal generator generates square waveform through the bias tee and the oscilloscope get the output signal.

Figure 3.4

The generator signal and the output signal through the bias tee. It presents that no distortion at 5.5 MHz, which means there is no waveform distortion within 100 ns range.

Figure 3.5

The generator signal and the output signal through the bias tee. It presents that the cutoff frequency happens at 100 KHz.

Figure 3.6

Equivalent circuit of the TDR experiment. The whole system including the bias tee, all cables, the sample and the sample holder is assumed to be a R-C series termination.

Figure 3.7

Source signal and reflection signal in the oscilloscope, which indicates that the attenuation is 5.

Figure 3.8

Typical TIPS sample dimensions. 3 mm*10 mm with thickness 0.2 mm.

Figure 3.9

Schematic of the setup of the fast photoresponse experiment. Full or narrow illumination is not indicated. The power supply polarity can be changed.

Figure 3.10

Noise level after noise reduction, which is 128 averages and takes roughly 110 seconds.

Figure 3.11

The baseline signal was deleted to get photoresponse signal.

Figure 3.12

The baseline signals at 6 minutes interval, which shows that the baseline shifts over time. The dashed line is wave form taken at 14:20 and the solid line is wave form taken at 14:26.

Figure 3.13

3-D laser beam Gaussian profile which shows that laser intensity is non-uniform.

Figure 3.14

X-axis Gaussian beam distribution with Gaussian radius fitted to 0.076 mm.

Figure 3.15

Y-axis Gaussian beam distribution with Gaussian radius fitted 0.79 mm.

Figure 4.1

Typical Photoresponse wave forms at positive electric field and negative electric field at room temperature. The laser power 5 mW in narrow beam case.

Figure 4.2

Typical photoresponse wave forms at different electric field. The wave forms were shifted up 0.5mV one by one from electric field=333 V/cm. The laser power is 5 mW and kept constant.

Figure 4.3

Typical photoresponse wave forms at different laser intensity at room temperature. The wave forms were shifted up 0.5 mV one by one from laser power=3 mW. The electric field is 1000 V/cm and kept constant.

Figure 4.4

Different sample wave forms which fit power-law decay formula $I(t) \sim t^{-\alpha}$ indicates dispersive transport behavior. Inset is a log-log plot which shows power-law decay. The straight line shows power=-0.5.

Figure 4.5

Photoresponse waveform shows system 46 ps rise time, which suggest that the charge carrier photogeneration is below this time range. Also the time constant calculation indicates that the rise time has no relation with sample dimensions due to the higher silver paste/Epoxy paste contact resistivity.

Figure 4.6

Photoresponse wave forms at 300 K and 77 K. The laser power and electric field are same in both cases. The solid line is photorresponse waveform at 300 K and the marked one is at 77 K.

Figure 4.7

The current-voltage curve of the SCLC experiment was fitted to formula $I-V^2$ to calculate the charge carrier mobility. The power-law fitting result is 2 and the mobility is $0.05 \text{ cm}^2 / V\text{cm}$ assuming no defects and traps inside crystals. However, the real value should be larger than this result because of the defects/traps and the effective electrical thickness.

Figure 4.8 (a)

Fast photoresponse waveform at 800 nm excitation wavelength for calculating the charge carrier photogeneration quantum efficiency and the mobility. The calculation mobility is $1.6 \times 10^{-4} \text{ cm}^2 / V\text{cm}$ which is really smaller than SCLC result because of the fast charge carrier recombination during 50 ps after photoexcitation.

Figure 4.8 (b)

Fast photoresponse waveform at 400 nm excitation wavelength for calculating the charge carrier photogeneration quantum efficiency and the mobility.

Figure 4.9

THz result presents the system response time is sub-picosecond and the photocurrent decays to 5% at 35 ps. Since the temperature, excitation wavelength are the same as fast photoresponse experiment and the weak external electric field can be neglected, all parameters in both experiments are the same, which indicates the charge carrier photogeneration and transport behavior are the same.

Figure 4.10

Photoresponse waveforms at focusing laser beam. The positive waveform is biased with negative electric field and the negative one is biased with positive electric field.

Figure 4.11

Photoresponse waveform of full illumination case. The time scale extends to 8 ns. In the other hand, in the narrow laser beam case as illustrated in Figure 4.10, the time scale within 1ns.

The different behaviors are due to the space charge effect and traps/defects. The positive waveform is biased with negative electric field and the negative one is biased with positive electric field.

Figure 4.12

Photoresponse peak dependence on electric field at 800 nm and 400 nm excitation wavelengths. The linear dependence suggests the charge carrier transport is ohmic and contact is ohmic contact. It is expected that at higher field the molecular excitons will dissociate due to the electric field.

Figure 4.13

Photoresponse peak vs. laser fluence at 800 nm and 400 nm excitation wavelengths. The super-linear and linear dependence at 800 nm and 400 nm excitation wavelengths respectively may indicate two-photon and one-photon absorption.

Figure 4.14

Normalized photoresponse waveforms biased with different electric fields. It does not present waveforms difference due to the weak electric field.

Figure 4.15

Photoresponse peak at different positions at positive, negative and zero biased electric fields. The peaks at zero electrical field indicate a built-in field exists at the metal/organic interface and direct from the TIPS to the gold. The non-symmetrical behavior is not clear so far.

Figure 4.16

The 800nm focusing laser beam which is smaller than electrode spacing scans different positions on surface of the crystal and the gold film. The arrows below are clearly to tell different scan regions.

Figure 4.17

Photoresponse waveforms at different positions biased with zero electric field. The fast decay behavior is due to the space charge effect since the space charge field weakens the built-in field, thus the charge carriers reach electrode or fall in traps rapidly. The very fast signal was limited by the system bandwidth.

Figure 4.18 (a)

Interface photoresponse wave forms biased with zero electric field at room temperature. Laser power is 2.88 mW.

Figure 4.18 (b)

Interface photoresponse wave forms biased with negative electric field at room temperature. Laser power is 2.88 mW.

Figure 4.18 (c)

Interface photoresponse wave forms biased with positive electric field at room temperature. Laser power is 2.88 mW.

Figure B (1)

Current-voltage plots of a typical insulator.

Figure C (1)

Electrode structure shows a single electrode bounded by equi-potential planes.

Figure C (2)

Transformed parallel planes with the corresponding image points indicated by the same lower case letters.

Figure D (1)

H parameter dependence on l_2 / l_1 in isotropic materials.

Figure D (2)

Normalized effective thickness dependence on normalized thickness in isotropic materials.

Figure E (1)

Sample dimensions.

Figure E (2)

Fast photoresponse waveform at 800 nm excitation wavelength.

Figure E (3)

Fast photoresponse waveform at 800 nm excitation wavelength.

Chapter 1 Introduction

- 1.1 Organic molecular crystals (Polyacenes)
- 1.2 The optical properties of organic molecular crystal
- 1.3 Functionalized pentacene (TIPS) chemical structure
- 1.4 Techniques for measuring transient photoconductivity
 - 1.4.1 The time domain pump-probe technique
 - 1.4.2 The time-of-flight technique
 - 1.4.3 The Auston switch technique

Chapter 1 Introduction

Organic molecular crystals like polyacenes including naphthalene [1, 2], anthracene [3], tetracene [4, 5], and pentacene [6-11] show promising application in electronics. The chemical structures of the polyacenes are illustrated in Figure 1.1. However, the mechanism of charge carrier photogeneration and transport has been a subject of controversy for two decades due to the complex nature of the problem. In this chapter we cover the topics including the general physical properties of polyacenes, their optical properties, functionalized pentacene single crystals which were investigated here, and several transient techniques to detect photoconductivity.

1.1 Organic molecular crystals (Polyacenes)

Organic molecular crystals differ considerably in their optical, electronic, and mechanical properties from such conventional solids as covalent or ionic crystals. This is mainly due to weak intermolecular interaction forces of the Van der Waals type with binding energies considerably lower than that of covalent or ionic bonds in atomic crystals. (Property comparisons between organic and inorganic covalent-bonded semiconductor crystal are listed in Table 1.1) In 1978 Uyeda *et al.* [12] got a superb electron micrograph of a molecular crystal as illustrated by Figure 1.2. The micrograph allows one to discriminate the image of

constituent atoms of every single molecule. However, the most important aspect of this microscopy is that the individual molecules are actually separated by “channels” with negligible electron density. From this aspect, organic molecular crystals are like an “oriented molecular gas” of isolated molecules. These almost electronless intermolecular “channels” give the visual picture of the weak, long-distance Van der Waals interaction forces. Such molecular electronic structure determines the basic specific features of optical and electronic properties of molecular crystals as well as peculiarities in their energy spectra for neutral and ionized states.

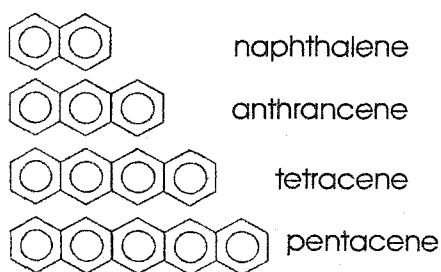


Figure 1.1
Chemical structures of polyacenes including naphthalene, anthracene, tetracene and pentacene.

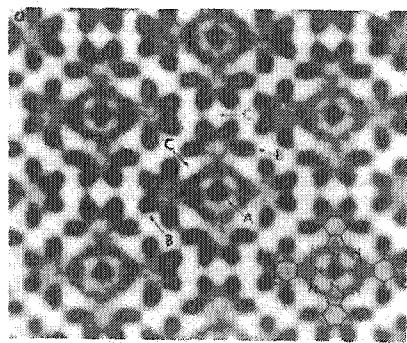


Figure 1.2
High resolution microscopy image of copper hexadecachlorophthalocyanine molecule in the $a-b$ plane of the crystal. (From Ref. 12)

**Table 1.1 Characteristic Features Comparison Between
Organic Molecular Crystals and Inorganic Covalent Bonded Semiconductors [12]**

Organic molecular crystal	Inorganic covalent semiconductor
Weak Van der Waals type of interaction (characteristic interaction energy $E = 10^{-3} - 10^{-2}$ eV)	Strong covalent-type interaction (characteristic interaction energy $E = 2 - 4$ eV)
Marked tendency of charge carrier and exciton localization	Pronounced charge carrier delocalization
Self-energy of charge carriers and excitons determined by many-electron interaction (polarization) effects	Single-electron approximation valid
Charge carriers and excitons as polaron-type quasiparticles	Charge carriers as free holes and electrons
Low charge carrier mobilities $\mu = 1 \text{ cm}^2 / \text{Vs}$ and small mean free path $l \approx a_0 =$ lattice constant at room temperature	High charge carrier mobilities and large mean free path $l = 100-1000 a_0$
Large effective mass of charge carriers $m_{eff} = (10^2 - 10^3)m_e$	Small effective mass of charge carriers $m_{eff} \leq m_e$
Hopping-type charge carrier transport dominant	Band-type charge carrier transport dominant
Frenkel excitons	Wannier excitons
Low melting and sublimation temperatures, low mechanical strength, high compressibility	High melting and sublimation temperatures, high mechanical strength, low compressibility

1.2 The optical properties of organic molecular crystals

Since weak intermolecular interaction forces produce only a slight change in the electronic structure of molecules on the formation of the solid phase and molecules in the lattice keep their identity, it's a good beginning to talk about the optical properties of a simple diatomic molecule. The optical properties of the coupled vibrational-electronic levels of a molecule can

be understood by involving the Franck-Condon principle [13], which states that the electronic transition takes place so rapidly that the nuclei do not move significantly during the transition. Basically, the Franck-Condon principle follows from the Born-Oppenheimer approximation, which claims that nuclei are fixed, and is a consequence of the fact that nuclei are much heavier than the electrons.

The processes when photons are absorbed and re-emitted by a molecule according to the Franck-Condon principle are illustrated schematically in Figure 1.3. The molecule starts in the ground state with a mean nuclear separation of r_1 . The absorption of the photon promotes an electron to the excited state without changing r . The transition thus leaves the molecule in the excited state with a mean nuclear separation of r_1 instead of the equilibrium separation of r_2 . Then the separation of the nuclei rapidly relaxes to r_2 before re-emitting a photon. This leaves the molecule in the ground state with a mean nuclear separation of r_2 . Further rapid relaxation processes occur to complete the cycle and bring the molecule back to its equilibrium separation in the ground state as Figure 1.3 shows. In summary, the absorption of a photon excites the molecule into an excited electronic state as well as an excited vibrational state. The excess vibrational energy is lost very rapidly through a non-irradiative relaxation process, as indicated by the dotted lines in Figure 1.3. Figure 1.4 is an example of absorption and emission spectrum of anthracene in solution.

The organic crystal spectrum completely keeps the spectral features of that of individual molecules, including their electronic-vibrational structure. Therefore the optical spectra of an isolated molecule and molecular crystal are similar. On the other hand, certain new optical and electronic properties emerge in the crystal spectra caused by a collective molecular interaction. Thus, due to dispersion and resonance interactions of the excited molecule with its local crystalline surrounding, the spectral bands show a long-wave shift (red shift) and such specific

phenomena as Davydov splitting, changes in the exciton bands caused by interaction with lattice phonons, *etc.*

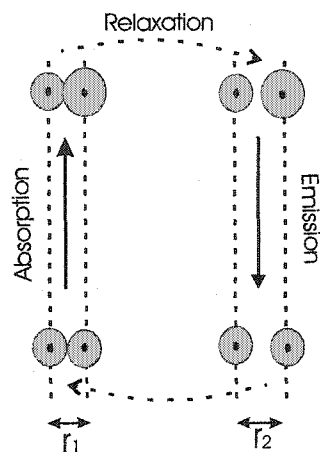


Figure 1.3

Schematic electronic transition processes in organic molecule, which include absorption, emission processes and relaxation as dotted line indicate. (Adapted from Ref. 13)

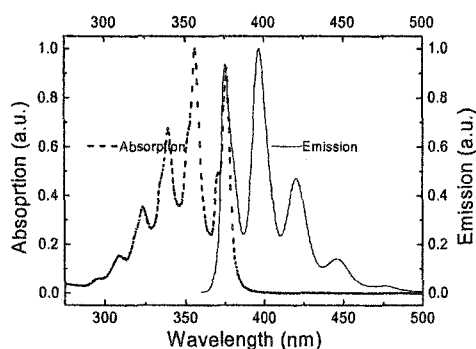


Figure 1.4

Absorption and emission spectra of anthracene. (Adapted from Ref.15)

1.3 Functionalized pentacene chemical structure

The parent pentacene crystal in Figure 1.5, adopting the well-known herring-bone structure, has attracted more attention in recent years. Functionalized pentacene (6,13 bis triisopropylsilylethynyl pentacene, hereafter TIPS) chemical structure is illustrated in Figure 1.6 [15-17], and it has side groups at a premier position of the pentacene, enhancing face-to-face interactions since the interplanar spacing of the aromatic ring is smaller than parent pentacene (6.27 \AA for parent pentacene, 3.47 \AA for functionalized pentacene) [18,19].

This increases the orbital overlap and π interaction throughout the solid. The TIPS crystal is more like a two dimensional brick structure (Figures 1.7 and 1.8), so it's reasonable to expect that the conductivity along the b -axis is much larger than along the c -axis, which is proved by Anthony *et al.* [15] Appendix A presents the parent and functionalized pentacene crystallographic data.

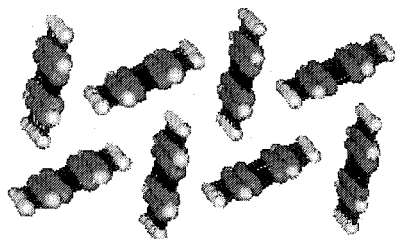


Figure 1.5
The well known parent pentacene herring-bone structure. (From Ref. 16)

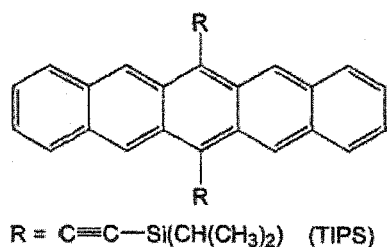


Figure 1.6
TIPS single molecule chemical structure.
R represents side groups. (From Ref. 15)

John E. Anthony recently synthesized other functionalized pentacene crystals and found that even with the increase of the π -orbital overlap, the conductivity is not significantly increased (John Anthony, private communication). The precise relationship between electric and structural properties, therefore, remains unclear.

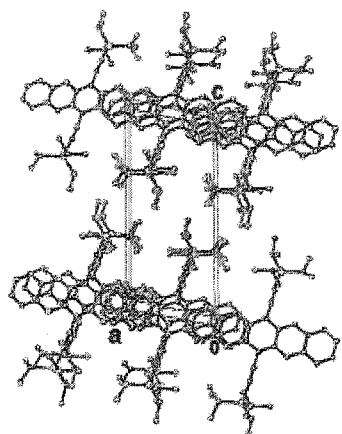


Figure 1.7
TIPS chemical structure. View along the crystallographic *b*-axis, corresponding to the π -stacking axis, showing two-dimensional stacks of TIPS molecules together with space filling views of the crystal packing. (J. E. Anthony, private communication)

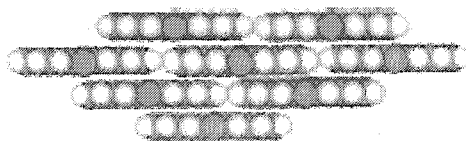


Figure 1.8
TIPS two-dimensional brick structure in the *a-b* plane. (From Ref. 16)

We use a coplanar electrode geometry on the TIPS crystal, which is similar to the Auston switch technique described in the next section, to detect the fast photoresponse of the TIPS crystal. The whole system response time is 50 ps which is comparable to other groups and shows that this technique is feasible to investigate the crystal's fast photoresponse behaviour. Compared to our experimental setup, there are several other transient techniques to investigate fast photoconductivity which will be discussed in the following section.

1.4 Techniques for measuring transient photoconductivity

1.4.1 The time domain pump-probe technique

Time domain pump-probe techniques have been applied to study ultrafast molecular phenomena in biology [20-22], chemistry, and solid state science [23-26] with temporal resolution in the picosecond and femtosecond range. As Figure 1.9 illustrates, the ultrafast temporal resolution is achieved by beam splitting a laser source to generate very short pulses into a pump beam and a probe beam and recombining the beams at the sample under investigation. By careful control of the optical paths of the pump beam and the probe beam, the arrival of the probe beam can be delayed relative to the pump beam by a chosen amount. The result is that the probe beam with the optical delay can detect carrier and molecular dynamics following the arrival of the first excitation beam. By varying the optical delay, the dynamics of the sample can be mapped at different times following the arrival of the initial excitation beam. The pump beam excites and depletes the molecules in the ground state. Later, the delayed probe beam arrives and probes the recovery of the ground state population. Any dynamic processes affecting the return of molecules back to the ground state can then be studied by monitoring the probe beam.

One of the pump-probe techniques is time-resolved terahertz spectroscopy, which employs a short duration THz probe pulse (a frequency around 10^{12} Hz) to study transient photoconductivity in materials. If the pump beam produces increased absorption of the probe beam in the sample, then the transmission peak T of the probe beam is decreased from its initial peak values of T_0 . If the differential transmission is defined as $\Delta T/T_0 = (T - T_0)/T_0$ and transient photoinduced absorption in the sample is represented as a function of probe delay time, for low mobility samples it can be shown that $-\Delta T/T_0 \propto ne\mu$, where n is the carrier concentration, e is the fundamental charge and μ is the effective carrier mobility. The advantage of this technique is that it is a non-contact measurement of transient photoconductivity and charge carrier photogeneration, transport, and relaxation.

Photogenerated carrier dynamics in pentacene single crystals [27] and functionalized pentacene single crystals [28] have been studied using terahertz pulse techniques.

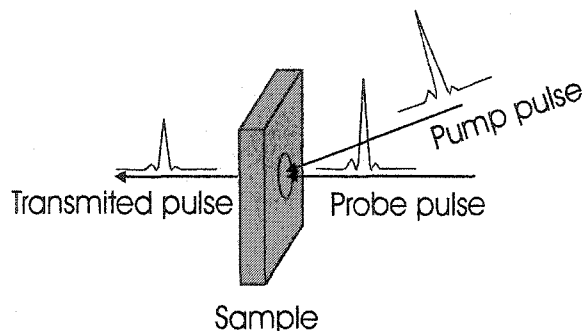


Figure 1.9
Schematic setup of the time domain pump-probe technique. A probe beam and pump beam are split from a single ultrafast laser source.

1.4.2 The time-of-flight technique

A useful technique for measuring the carrier mobility in any material is the time-of-flight (TOF) method of Kepler [29]. Figure 1.10 shows the usual experimental setup for observing time-of-flight signals. A sample of length L is provided with two electrodes (one semi-transparent) in a sandwich arrangement. The carriers are generated by pulsed light incident on the semi-transparent electrode and absorbed in a skin depth that is much less than L . The sheet of carriers created is then transported across the sample under the action of an applied field. As they drift, they induce a time-dependent current $I(t)$ in the external circuit which is observed. When the carriers reach the other electrode and discharge, $I(t)$ drops suddenly, and it is the time of this transition region that is taken as the transit time. The carrier transport can be classified into two categories [30]:

- 1) Gaussian propagation. The carrier packet broadens symmetrically about its mean position as it transverses the sample length. The peak of the packet and the mean position are located at the same position and move with the same constant velocity. Gaussian statistics predicts a linear dependence of t on diffusion length and such

propagation has been observed in crystals such as naphthalene and anthracene at low temperatures.

- 2) Non-Gaussian propagation or dispersive propagation. In this case, the carrier packet undergoes a significant broadening as it drifts through sample, so Gaussian statistics can no longer be applied. The peak of the packet remains fixed at the point of origin of the carrier and the position of the mean separates from the peak and moves with a velocity that decreases with time. Such broadening is usually associated with considerable disorder in the sample. It predicts a non-linear length dependence of time on diffusion length and it is dispersive propagation.

For the ideal case where the carrier sheet undergoes no dispersion as shown in Figure 1.11(a) the current exhibits a sharp drop. On the other hand, because of the charge carrier dispersion transport discussed above, the wave form will exhibit a tail with the width of the tail a measure of the degree of this dispersion. This case is shown in Figure 1.11(b). Taking the position of the shoulder indicating the transit time, which can be obtained by log-log scale of the waveform as Figure 1.11(c) shows, an unambiguous drift velocity and mobility for the faster carrier may be determined from the relationships $v_d = L/t_\tau$ and $\mu = v_d / E$, where t_τ is transit time, v_d drift velocity and E electrical field. By reversing the polarity of the applied field, the drift and carrier mobility for the other sign of carriers may be deduced. In 1985, N. Karl's group [31] used TOF technique to investigate ultrapure naphthalene and detected the charge carrier non-dispersive transport at temperatures.

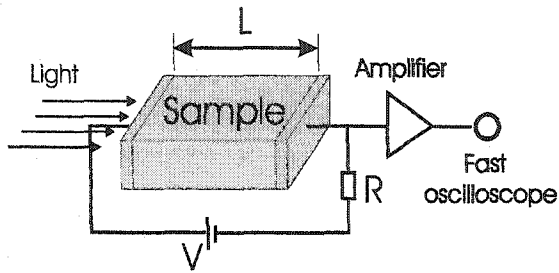


Figure 1.10

Schematic setup of the time-of-flight technique. The absorption thickness is much smaller than sample thickness.

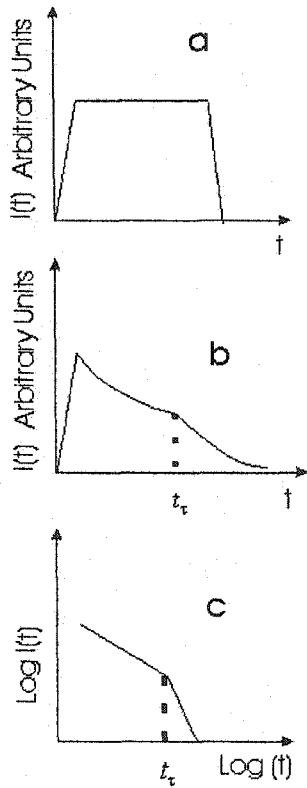


Figure 1.11

- a) Ideal TOF current wave form without dispersion.
- b) Wave form with charge carrier dispersion. The sharp tail in the ideal case becomes longer and the shoulder indicates the transit time.
- c) Log-log scale of wave form b to get the transit time t_r indicated by the dashed line.

1.4.3 The Auston switch technique

The Auston switch technique was developed by David Auston in 1983 and detects fast photoconductivity in semiconductors [32]. This geometry is presented in Figure 1.12. In order to match the impedance of the coaxial cables, a $50\ \Omega$ microstrip transmission line is used. The capacitance is significantly reduced by the fact that it is distributed along the transmission line rather than being lumped at the surface of a parallel-plate capacitor. Traditionally, the photoconducting circuits were made by depositing a thin film of material under investigation on a substrate like silica. Then a very thin film of aluminum or gold is evaporated through a

mask onto the thin film in the form of a microstrip. To complete the transmission line, a uniform aluminum/gold layer is evaporated on the bottom surface of the substrate. The gap between the microstrips is of the order of $10\sim 100\ \mu\text{m}$. When light is focused on this gap, a conducting path that enables a current to flow across the gap is formed. The capacitance of the gap is really small because of the end-on configuration of the electrode which significantly reduces the system rise time. People have used this technique to observe photoconductivity of amorphous-silicon [33], C60 [34], polydiacetylene [35], *etc.*

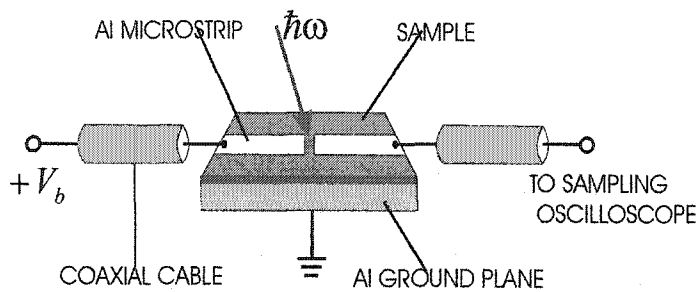


Figure 1.12
Schematic setup of the Auston switch technique. The system response time can be sub-nanosecond.

Chapter 2 Charge carrier photogeneration and transport mechanisms in organic molecular crystals

- 2.1 Charge carrier photogeneration mechanisms
 - 2.1.1 Molecular exciton model
 - 2.1.2 Semiconductor band model
 - 2.1.3 Electric field dependence according to the Onsager model
- 2.2 Charge carrier transport
 - 2.2.1 Charge carrier transport mechanisms
 - 2.2.2 Electrical field dependence
- 2.3 Impacts of traps
- 2.4 Metal semiconductor junctions –The Schottky barrier

Chapter 2 Charge Carrier Photogeneration and Transport Mechanisms in Organic Molecular Crystals

The nature of charge carrier transport in organic crystals is not clearly understood so far. The charge carrier mobility in ultrapure crystals demonstrates power law temperature dependence ($\mu \sim T^{-n}$), which is similar to inorganic semiconductor band transport behavior [12, 36, 37]. However, within this temperature range the mean free path of the charge carrier is the same order as the lattice constant, which might make thermally activated hopping model valid. Also there is controversy about the charge carrier photogeneration mechanism. In the semiconductor band model [12, 37], the primary photoexcitations are delocalized polarons generated directly by light absorption. On the other hand, the molecular exciton model [12, 38] claims that the excitons are the primary photoexcitations which are bounded but can be dissociated by an electric field or other mechanisms. In this chapter, we will talk about charge carrier photogeneration models and charge carrier transport mechanisms. Also, charge carrier photogeneration and transport processes, and how they are related to some parameters like

electric field, wavelength and temperature, will be discussed. At last we briefly mention the role of traps, defects and interface effects in our particular coplanar electrode geometry.

2.1 Charge carrier photogeneration mechanisms

2.1.1 Molecular exciton model

Charge carrier photogeneration phenomena have been most thoroughly studied in organic molecular crystals. A popular model is a multi-step photogeneration model [12] which involves various intermediate stages whose schematic transition is shown in Figure 2.1. The first stage is photon absorption and formation of a neutral Frenkel exciton state according to this model. Then autoionization of the excited molecular state takes place, with quantum efficiency $\Phi_0(h\nu)$, and creates a positively charged parent ion and a hot electron with excess energy. Due to fast inelastic scattering, the hot electron loses its initial excess energy and becomes thermalized at a mean thermalization length r_{th} inside the critical Coulombic radius r_c ($r_{th} < r_c$), thus forming an intermediate charge pair state of bound charge carriers at the third stage. At the final stage, free carriers are created via dissociation of the charge pair state and the dissociation probability can be described by the modified Onsager model.

After autoionization, the motion of the hot electron may be coherent. However, its coherent motion may be rapidly lost because of inelastic scattering from acoustic and optical lattice phonons, and the scattering events take place at every site. Thus the electron becomes strongly localized and further energy relaxation presumably occurs in an incoherent motion by hopping from site to site until it finally thermalizes at the distance r_{th} . After thermalization the charge pair state can either dissociate, forming free charge carriers, or undergo geminate

recombination. The Onsager theory allows us to determine the probability of these processes at a given temperature and an electric field strength E , which will be discussed in next section.

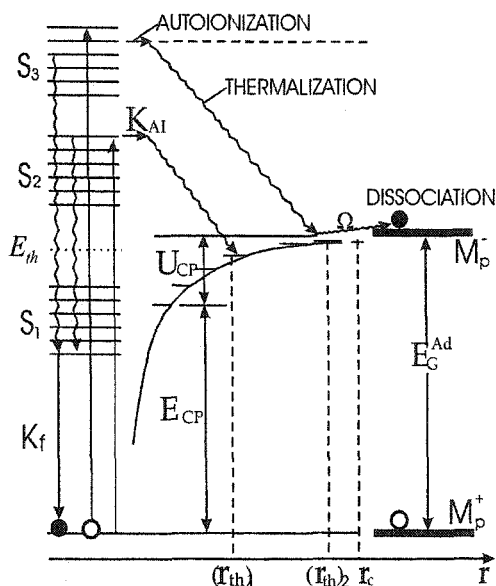


Figure 2.1

Multi-step photogeneration process in an organic molecular crystal which includes absorption, autoionization, thermalization, and dissociation. (Adapted from Ref. 12)

S_1, S_2, S_3 : excited electronic states

K_f : rate constant of radiative intramolecular relaxation

K_{AI} : rate constant of direct autoionization

E_G^{Ad} : adiabatic energy gap

E_{CP} : energy of charge pair, E_{th} : threshold energy, U_{CP} : Coulombic binding energy of charge pair, Ω : dissociation probability of charge pair state, r_{th} : mean thermalization length of hot charge carriers, M_p^+, M_p^- : molecular polaron states

2.1.2 Electric field dependence according to the Onsager model

In our experiment, we investigated the photoresponse peak dependence with electric field and temperature to figure out the photogeneration process involved and the quantum efficiency of the charge pair dissociation. In the Onsager model, the quantum efficiency of charge carrier photogeneration is a function of temperature, electric field and the excitation wavelength. According to this model, the activation energy for the probability of charge carrier geminate escape, i.e., activation energy of intrinsic photogeneration E_a^{ph} is determined by the Coulombic binding energy U_{CP} of the charge pair state.

$$E_a^{ph} = -U_{CP} = e^2 / 4\pi\epsilon\epsilon_0 r_{th} \dots\dots\dots 2.1$$

Thus by measuring the spectral dependence of the photogeneration activation energy $E_a^{ph}(h\nu)$ in a crystal, it is possible to evaluate the spectral dependence of the defined mean thermalization length $r_{th}(h\nu)$:

$$r_{th}(h\nu) = e^2 / 4\pi\epsilon\epsilon_0 E_a^{ph}(h\nu) \dots\dots\dots 2.2$$

The mean thermalization length of the charge carriers is dependent on $h\nu$, electric field E and the temperature T ; namely $r_{th} = r_{th}(h\nu, E, T)$. Also the quantum efficiency of free charge carrier photogeneration Φ is a function of photon energy, electric field and temperature and may be represented as a product of two probabilities: the charge pair state photogeneration quantum yield $\Phi_0(h\nu)$ and charge pair state dissociation efficiency Ω .

$$\Phi(h\nu, E, T) = \Phi_0(h\nu)\Omega[r_{th}(h\nu, E, T), E, T] \dots\dots\dots 2.3$$

Therefore, the parameters E and T influence both thermalization and dissociation stages of photogeneration in organic molecular crystals.

Based on the modified Onsager model, the electric field affects different electronic processes which are directly or indirectly connected with the photogeneration process or measurements of its parameters. The most important electronic process directly affected by the electric field, is the E -dependent charge pair state dissociation efficiency. In this case, the influence of the electric field due to the E -dependent term of the formula 2.3, begins at $E > 10^3 V/cm$. On the other hand, $\Omega(E)$ approaches the saturation value of unity at $E > 10^5 V/cm$. Also, the electric field can change the effective thermalization length r_{th} due to drift of hot electrons during thermalization. This effect can be observed at field strengths of $E > 10^5 V/cm$ and for sufficiently great mean thermalization lengths $r_{th} \geq 40 \overset{0}{\text{Å}}$. For still higher

electric field values, the situation arises when $r_{th} \geq r_c$ and the carrier moves out of the Coulombic field as a free thermalized carrier, or as a hot carrier with drift velocity v_d greater than the mean thermal velocity v_{th} . In this electric field range the microscopic mobility becomes field dependent, that is $\mu_0 = \mu_0(E)$, a characteristic feature of a hot carrier generation regime. In our case, the electric field is very weak, approximately $10^3 V/cm$, so charge pair dissociation due to the field may not be significant.

2.1.3 Semiconductor band model

Besides the molecular exciton model, a semiconductor band model [12,37] has also been proposed. Basically, the photoexcitations are mobile carriers which are created directly by the absorption of light. The process implies that the absorbed photons create directly electron-hole pairs due to interband transitions. In other words, the onset of the optical absorption at the band energy is the same as the onset of the photoconductivity. The process generally occurs in inorganic semiconductors and also occurs to a much less extent in organic semiconductors. This model can be proved by Chaiken and Kearns' experiment [37]. Their results on the spectral response of D.C. hole and electron photocurrent in anthracene are shown in Figure 2.2. It can be seen that in the spectral range 310-400 nm, both the hole and electron photocurrent curves resemble the absorption curves. However another group reported that in anthracene crystals the photogeneration follows the molecular exciton model, which can be proved by the spectral dependence of photocurrent quantum efficiency as Figure 2.3 exhibits [12], where the onset photocurrent happens at a wavelength 318 nm (3.9 eV), which is due to dissociation of tightly bound molecular excitons, while the onset of Chaiken's result is at a lower energy (3.1 eV).

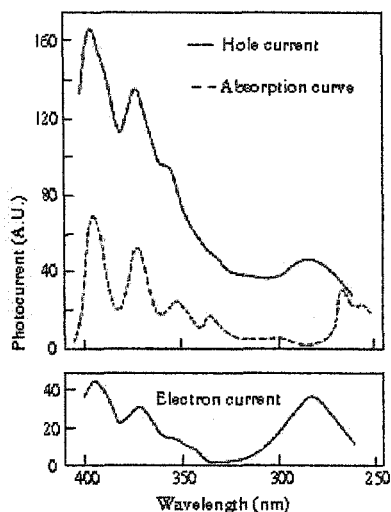


Figure 2.2

Spectral response of hole and electron photocurrents in anthracene at a temperature of 179 K. Applied voltage: 300 V D.C.; specimen thickness: 0.5mm; light intensity: 6×10^{12} photons/sec. The arbitrary photocurrent units are the same for both hole and electron curves. (From Ref. 37)

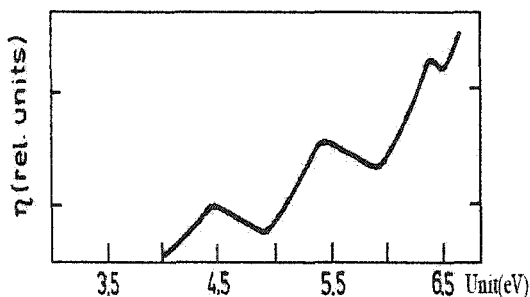


Figure 2.3

Spectral dependence of photocurrent quantum efficiency in anthracene single crystals. (From Ref. 12)

2.2 Charge carrier transport

2.2.1 Charge carrier transport mechanisms

In the low temperature range, the electron and hole mobility in polyacene crystals increases with decreasing temperature and the mobility follows the formula $\mu \propto T^{-n}$ ($0 < n < 2.9$), which is similar to charge carrier band transport behavior in inorganic semiconductors. However, the charge carriers mean free path l_0 is of the same order as the lattice constant. In other words, the charge carrier is scattered at every site and the band-like transport model is not valid in this case. The charge carriers are hopping site to site, so another model, the hopping model has been proposed, which predicts that the charge carrier mobility

follows the formula $\mu \propto \exp(-E_a/KT)$, where E_a is activation energy and K is Boltzmann constant. The work of N. Karl *et al.* [39] and L. B. Schein *et al.* [40] maybe prove the above models. Figure 2.4 is the electron mobility along c' direction in naphthalene crystals. It can be seen that below 100 K, the electron mobility can be fit to the formula $\mu \propto T^{-n}$ ($n=1.7$) and from 100 K to 150 K the electron mobility keeps constant, where N. Karl [12] claimed the band-like transport to hopping transport transition. The same mobility behavior was reported by L. B. Schein [40] in naphthalene crystals. The electron mobility along the c' direction in naphthalene crystals can be divided into three regions. 1st below 100 K, the electron mobility increases with decreasing temperature and follows the band transport model, 2nd, 100 K-150 K, the electron transport follows band transport to hopping transport transition, 3rd, 150 K-324 K, the electron mobility is independent of temperature and the electron transport follows the hopping model. The charge carriers' behavior along the a direction in naphthalene crystals follows the band transport model, which was shown by N. Karl *et al.* work in 1985 (Figure 2.5). The electron and hole mobility can be fitted to the formula $\mu \propto T^{-n}$, where $n = 1.4$ for electrons and $n = 2.9$ for holes, which is band-like transport. Charge carrier mobility in tetracene was studied by A. Szymanski *et al.* in 1969 [41] and recently by R. W. I. de Boer *et al.* [42], who employing spaced charge limited current (SCLC) and time-of-flight techniques. They found the hole mobility increases with decreasing temperature from room temperature to 425 K. For pentacene crystals, Palstra's group [43] reported that the charge carrier mobility follows the band transport model with $n = 2.38$ within temperature range from 225 K to room temperature. A. J. Taylor *et al.* [44] used time-resolved terahertz spectroscopy techniques to get the charge mobility in pentacene from 4K to room temperature following $\mu \propto T^{-n}$ ($n = 0.27$). However, T. N. Jackson's group [45] reported temperature-independent charge carrier mobility in pentacene from field-effect mobility measurement on

different pentacene-film transistors, which were grown under the same conditions. Figure 2.6 is the field-effect mobility dependence on temperature for three samples. From the graphs, it can be seen that the mobility of sample (a) can be fitted to formula $\mu \propto \exp(-E_a / KT)$, which follows the hopping model. However, the sample (c) mobility is independent of temperature, which indicates the hopping model may not be valid.

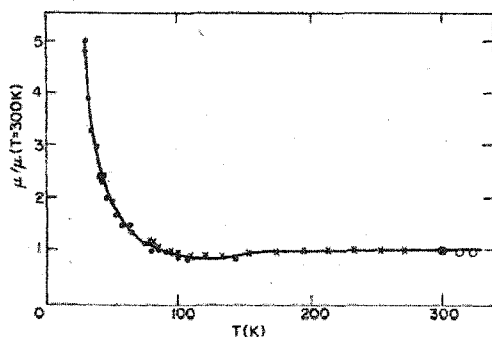


Figure 2.4

The temperature dependence of the electron mobility along the c' direction in naphthalene single crystals. The first part of the curve at low temperatures can be fitted to $\mu \propto T^{-n}$ ($n = 1.7$), which follows the band transport model. (From Ref. 31)

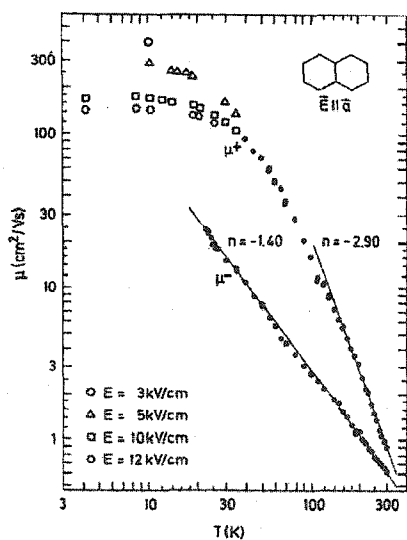


Figure 2.5

Electron and hole mobilities along the a -axis direction in ultrapure naphthalene versus temperature. The solid line indicates a T^{-n} power-law temperature dependence with exponent n as indicated in the figure. $\mu^- \propto T^{-1.4}$ for electrons and $\mu^+ \propto T^{-2.9}$ for holes. (From Ref. 39)

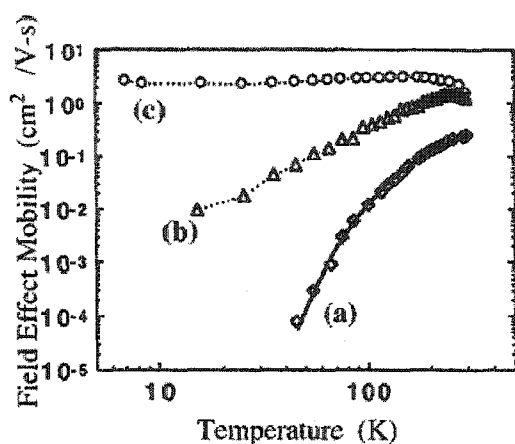


Figure 2.6

Field-effect mobility dependence on temperature for three different pentacene thin film transistors, which were made under the same conditions. Curve (a) was fitted to the formula $\mu \propto \exp(-E_a / KT)$ and $E_a = 38 \text{ meV}$. It clearly shows that curve (c) is independent of temperature. (From Ref. 45)

In summary, the charge carrier transport behavior in polyacene crystals is not clear so far and it is not simple to address the charge carrier transport mechanism, even if the crystal under investigation is the same, as seen from the results of different research groups studying pentacene. The way to clarify it is to study the charge carrier mobility in different temperatures. The low temperature fast photoresponse experiment was tried in our case. However, due to the sample cracking at low temperature, the signal was not reproducible. It maybe feasible to perform low temperature experiments in the future.

2.2.2 Electrical field dependence

The conductivity dependence on electrical field consists of linear, sublinear and saturation regions. This behavior can be interpreted in terms of field-induced specific scattering mechanisms of the charge carriers off of acoustic and optical phonons of the lattice. In the state of thermal equilibrium, the carrier's relaxation time τ_r is assumed to be isotropic and constant. In this case, mobility μ is constant and field-independent at a given temperature. However, at higher electric fields, the field-induced charge carrier's velocity components become comparable to the thermal velocity. As a consequence, the mean scattering time τ_r

becomes markedly reduced due to acceleration of the carrier in the electric field resulting in a faster approach to the scattering sites. This effect is the principal cause for field-induced non-linearity of carrier transport, observed as a field-dependent decrease in mobility. Thus there are two critical field values to be assigned. The first one, E_c , at which $v_d(E) \approx v_{th}$, and the sub-linear deviation from Ohm's law starts due to the beginning of field-induced hot carrier generation in the acoustic scattering range. The second threshold value of E , namely $E = E_s$, can be assigned to the onset of dominant scattering off of optical phonons from which the saturation region of the $v_d(E)$ dependence starts. Another important conclusion may be derived from the observed $v_d(E)$ dependence of hot charge carrier transport. At sufficiently low temperature and high electric field the charge carriers reach a drift velocity much higher than both the mean thermal velocity of the carrier ($v_d(E) > v_{th}$) and the longitudinal sound velocity μ_L ($v_d(E) > \mu_L$). This fact excludes all those lattice polaron model concepts where a charge carrier must be preceded by lattice distortions which prepare resonant sites [40]. However, it is demonstrated that both thermalization and hot carrier transport and the dependence of their effective masses on temperature may be described in the framework of the nearly small molecular polaron model [12].

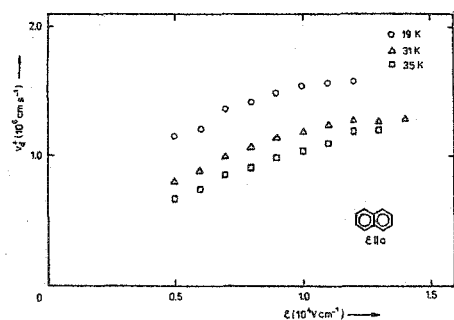


Figure 2.7

Hole drift velocity dependence on electric field in the a -direction of a naphthalene crystal. It shows the hole drift velocity saturate when the electric field is above 1.5×10^4 V/cm. (From Ref. 12)

2.3 The impact of traps

Impurities and traps [30] in an organic molecular crystal can significantly affect charge carrier mobility. However, in practice, the most studied cases are crystals with defects and traps. Thus it is worthy to mention the traps in a crystal which affect charge carrier transport in our case. A trap is an impurity atom or other imperfection in the crystal capable of capturing an electron or hole; the captured carrier may be re-emitted at a subsequent time. There is an operational distinction between two types of traps: one type acts principally as a recombination center, helping electrons and holes to recombine and thereby assisting in the restoration of thermal equilibrium; another type of trap does not contribute directly in an important way to recombination, but affects principally the energy distribution and freedom of motion of charge carriers of one sign. The first type of trap leads to the rapid decay of the photocurrent before the carriers reach the electrode and the second type of trap leads to multiple trap-limited photocurrent decrease and an increased thermally-activated effective transit time. The charge carrier transport behavior in the TIPS crystal we investigated is incoherent probably due to traps or defects which will be discussed in Chapter 4.

2.4 Metal-semiconductor junctions –The Schottky barrier

In our experiment, we evaporate 120 nm gold films onto TIPS which forms a metal/organic junction, so the behavior of the junction is of concern in our case. However, we have no definite theory for discussing the metal/organic junction. We can get an understanding of these junctions based on Schottky barrier theory about metal/semiconductor junctions. To see how a Schottky barrier may form when a metal comes into contact with a semiconductor, suppose that the metal and semiconductor are both electrically neutral and separated from each other. The energy-band diagram is shown in Figure 2.8 (a) for an n-type semiconductor with a

work function less than that of the metal; this is the most important case in practice, and we suppose that there are no surface states present. If the metal and semiconductor are connected electrically by a wire, electrons pass from the semiconductor into metal and the two Fermi levels are forced into coincidence as shown in Figure 2.8 (b). The energies of electrons at rest outside the surfaces of the two solids are no longer the same, and there is an electric field in the gap directed from right to left. There must be a negative charge on the surface of the metal balanced by a positive charge in the semiconductor. The charge on the surface of the metal consists simply of extra conduction electrons contained within the Thomas-Fermi screening distance ($\sim 0.5 \text{ \AA}$). Since the semiconductor is n-type, the positive charge will be provided by conduction electrons receding from the surface, leaving uncompensated positive donor ions in a region depleted of electrons. Because the donor concentration is many orders of magnitude less than the concentration in the metal, the uncompensated donors occupy a layer of appreciable thickness w , comparable to the width of the depletion region in a p-n junction, and the bands in the semiconductor are bent upwards as shown in Figure 2.8 (b). The difference V_i between the electrostatic potentials outside the surfaces of the metal and the semiconductor is given by $V_i = \delta \varepsilon_i$, where δ is their separation and ε_i is the field in the gap. If the metal and semiconductor approach each other, V_i must tend to zero if ε_i is to remain finite (Figure 2.8 c) and when they finally touch (Figure 2.8 d), the barrier due to the vacuum disappears altogether and we are left with an ideal metal-semiconductor contact. It is clear from the fact that V_i tends to zero that the height of the barrier is $\phi_b = \phi_m - \chi_s$.

In most practical metal-semiconductor contacts, the ideal situation shown in Figure 2.8 (d) is never reached because there is usually a thin insulating layer of oxide on the surface of the semiconductor. A practical contact is therefore more like that shown in Figure 2.8 (c); however, the barrier presented to electrons by the oxide layer is usually so narrow that

electrons can tunnel through it quite easily, and Figure 2.8 (c) is almost indistinguishable from Figure 2.8 (d) as far as the conduction electrons are concerned. Moreover, the potential V_i in the oxide film is so small that $\phi_b = \phi_m - \chi_s$ is still a very good approximation. Other types of semiconductor and metal junction band geometries can be obtained in the same way.

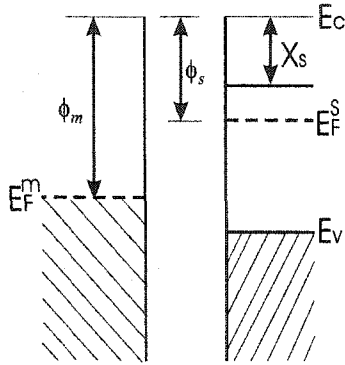


Figure 2.8 (a)

Band diagram of isolated metal and semiconductor. The Fermi level of metal is higher than the N-type semiconductor Fermi level

- E_F^m : Metal Fermi level;
 - E_V : Semiconductor valence band
 - E_C : Semiconductor conduction band
 - ϕ_m : Metal work function;
 - X_s : Semiconductor work function;
 - ϕ_s : Work function difference
- (Adapted from Ref. 46)

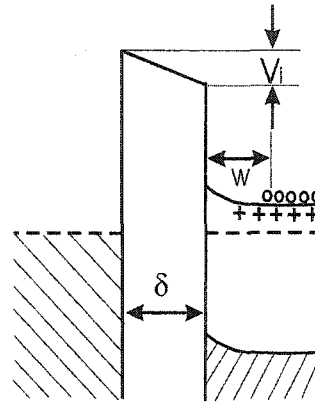


Figure 2.8 (b)

Band diagram of isolated metal and semiconductor which are electrically connected.

- δ : Separation between metal and semiconductor
 - W : Depletion layer
 - V_i : Electrostatic potential difference between metal and semiconductor
- (Adapted from Ref. 46)

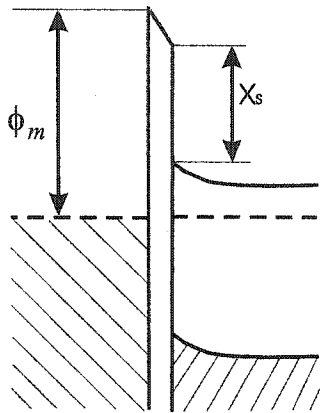


Figure 2.8 (c)
 Band diagram of isolated metal and semiconductor which are separated by a narrow gap.
 (Adapted from Ref. 46)

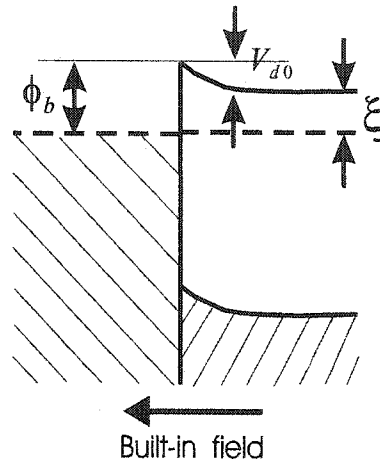


Figure 2.8 (d)
 Band diagram of isolated metal and semiconductor which are in perfect contact.

$$\phi_b = \phi_m - X_s$$

$$\zeta = E_C - E_F^S$$

(Adapted from Ref. 46)

- Chapter 3 Sample preparation and experimental setup
- 3.1 Sample preparation
 - 3.1.1 Shadow mask and gold bulk cleaning
 - 3.1.2 Pumping procedure for diffusion pump systems
 - 3.1.3 Sample mounting
- 3.2 Electrical components bandwidth test
- 3.3 Experiment setup
- 3.4 Noise reduction
- 3.5 Laser beam profile

Chapter 3 Sample Preparation and Experimental Setup

In this chapter, we mainly talk about some experimental work like sample preparation, electrical component bandwidth tests, and noise reduction technique.

3.1 Sample preparation

3.1.1 Shadow mask and gold bulk cleaning

To achieve good adherence between the sample and gold film, the bulk gold and shadow mask should be thoroughly cleaned both chemically and physically before evaporation. All components of the shadow mask were taken apart and immersed in water in the ultrasonic cleaner for half an hour, then all parts were dried with hot air. Finally all parts were cleaned with methanol and acetone. The same cleaning process was used for bulk gold. After all parts were cleaned, a clean copper wire was put in the center of the shadow mask to make a gap (330 μm) and nitrile gloves were worn to put the TIPS single crystal sample on the shadow mask carefully because the TIPS crystal is very brittle, then all parts were put on the work holder in the bell jar chamber.

3.1.2 Pumping procedure for diffusion pump system

The procedure for pumping the bell jar is very important for sample preparation. Due to the diffusion pump, oil may be sucked into the bell jar resulting in low evaporation quality. It is recommended to pump below 3×10^{-7} Torr. Another important thing to keep in mind is that everything inside the bell jar should be cleaned thoroughly. A schematic of the vacuum pump system is shown in Figure 3.1 and the following is the detailed pump procedure.

Pump down from atmosphere

The system should be found in the following condition if the bell jar is at atmosphere:

1. The diffusion pump is ON.
2. The foreline valve (backing valve) is OPEN. Foreline pressure should read approximately 10 to 50 millitorr.
3. The roughing line is CLOSED.
4. The gate valve (high vacuum valve) is CLOSED.
5. The vent valve is OPEN.

To pump the system to high vacuum:

1. Fill the liquid nitrogen trap with LN₂.
2. Ensure the vent valve is CLOSED.
3. CLOSE the foreline valve.
4. OPEN the roughing valve.
5. Rough the bell jar down to approximately 75 millitorr. DO NOT rough any further than 50 millitorr. Once the bell jar pressure is at 75 millitorr, CLOSE the roughing valve and OPEN the foreline valve.
6. OPEN the high vacuum valve (gate valve) slowly; ensuring the foreline pressure does not exceed 150 millitorr.

7. Once the bell jar pressure reaches zero and the foreline pressure has recovered (to around 10 to 50 millitorr), turn on the high vacuum gauge. Once the pressure reaches the low 10^{-5} Torr range, turn on the degas switch. Allow system to pump down. After 15 to 20 minutes, turn off the degas switch.

Venting the system:

The system should be found in the following condition if the bell jar is at high vacuum

1. The gate valve (high vacuum valve) is OPEN (the trap should be filled with LN2).
2. The foreline valve is OPEN (foreline pressure should read 10-50 millitorr).
3. The roughing valve is CLOSED.
4. The vent valve is CLOSED.
5. The high vacuum gauge is ON.

To vent the system from high vacuum:

1. Turn off the high vacuum gauge.
2. CLOSE the high vacuum valve (gate valve).
3. OPEN the vent valve.
4. Allow the bell jar to vent. After a few minutes, the bell jar can be removed.

Leave the bell jar in vacuum:

1. Roughing valve is CLOSED (bell jar pressure at 500 millitorr).
2. Foreline valve is OPEN (foreline pressure should read 10-50 millitorr).
3. High vacuum valve is CLOSED.
4. Vent valve is CLOSED.

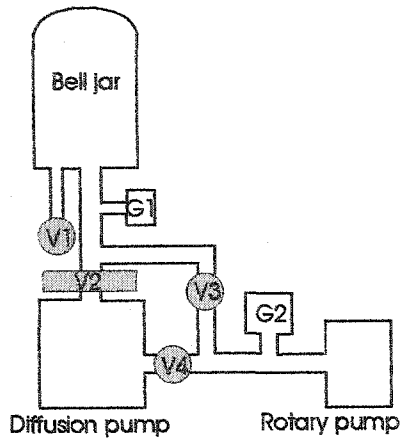


Figure 3.1

Schematic setup of evaporation system:

V1: Vent Valve

V2: Gate Valve

V3: Roughing Valve

V4: Foreline Valve (Backing valve)

G1: Penning Gauge

G2: Thermotron Gauge

3.1.3 Sample mounting

A $5\text{mm} \times 5\text{mm}$ PC board holder was made which had a $1\text{mm} \times 3\text{mm}$ slit in the center (Figure 3.2) to improve thermal contact between the crystal and the cold finger. SMA connector electrodes were soldered to the PC board copper. To prevent the sample from flipping around the board when the sample was pasted to the board copper using silver paste/epoxy paste (Circuitworks, Model CW2400), we first gently pasted one side of the gold film to the board copper, we then waited several minutes for the silver paste to stick and pasted the other side. All the work was done under a stereo microscope.

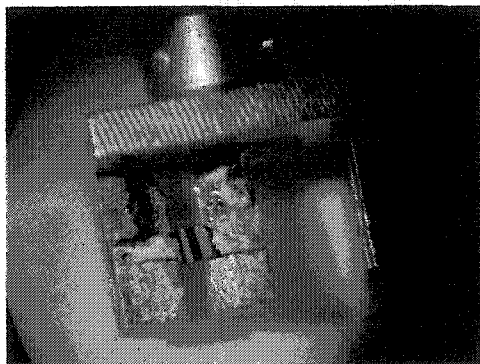


Figure 3.2

Picture of the sample, PC board sample holder and SMA connector. The sample is pasted on the PC board slit using conducting Epoxy paste. The copper on the PC board is soldered with the SMA electrodes.

3.2 Electrical components bandwidth test

The electric components in our experiment included the sample, coaxial cables, a bias tee and a fast oscilloscope. Due to the fast photoresponse signal, which extends to the sub-nanosecond range, the corresponding Fourier spectrum extended to very high frequency (~ GHz). This requires that all electrical parts are high frequency components (high bandwidth) ensuring that the original signal is not attenuated or distorted. The overall bandwidth of the electrical parts is limited by the smallest bandwidth component in all the devices. Our coaxial cable bandwidth is 18 GHz, the bias tee is 20 GHz and the oscilloscope is 40 GHz, so we expect the whole bandwidth is around 18 GHz. However, the real system bandwidth was smaller than 18 GHz due to numerous electrical connections between various parts of the system and the sample holder geometry itself. The bandwidth can be translated into rise time using the following formula

$$\tau_{rise}(ps) = \frac{350}{Bandwidth(GHz)} \dots\dots\dots 3.1$$

From the measured photoresponse signal the rise time was around 50 ps which means the system bandwidth was 7 GHz. This is smaller than the expected value of 18 GHz.

We used a signal generator to test the bandwidth of the bias tee. A bias tee consists of a capacitor, which isolates the D.C. bias from the oscilloscope, and inductor, which isolates the A.C. transient response from the D.C. power. It has a lower cutoff frequency (65 KHz) which may distort our signal at longer time scales in the microsecond range, so we used a signal generator to produce square signals (frequency up to 5.5 MHz) to test the bias tee cutoff frequency. Figure 3.4 & 3.5 present the generator signal and the output signal through the bias tee at 100 KHz and 5.5 MHz. Clearly, the input and the output signal are the same and no

distortion happened at 5.5MHz, which means that within 100 ns time scale, the photoresponse signal had no distortion.

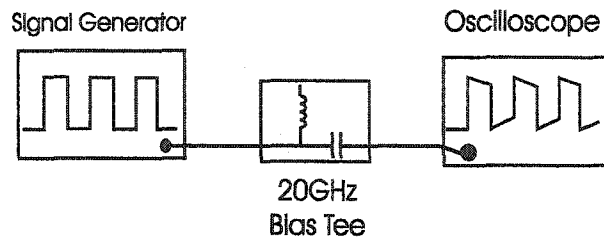


Figure 3.3
Simple experimental setup for testing the bias tee bandwidth.

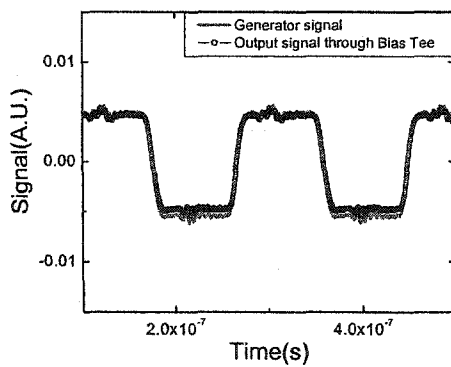


Figure 3.4
Generator signal (5.5 MHz) and output signal through the bias tee showing no distortion.

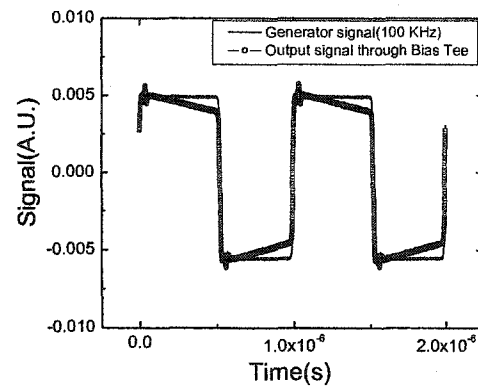


Figure 3.5
Generator signal and output signal through the bias tee which shows the cutoff frequency even happens at 100 KHz.

Also we employed the time domain reflectometry (TDR) technique [47, 48] to test the whole electrical system attenuation and bandwidth. TDR works on the same principle as radar. When a pulse of energy is transmitted down a cable and the pulse reaches the end of the cable, or a fault along the cable, part or all of the pulse energy is reflected back to the instrument. The TDR measures the time it takes for the signal to travel down the cable and reflect back off a discontinuity in the cable impedance. The TDR then converts this time to distance and

displays the information as a wave form or distance reading. Figure 3.6 shows the experimental setup for TDR measurements. A known fast signal from a fast photodiode is used as the input signal, and the reflection signal, which passes through the bias tee, all the coaxial cables, and the sample, displayed on the fast oscilloscope as shown in Figure 3.7. From the source to the reflection signal peak ratio, we get the attenuation to be 5.

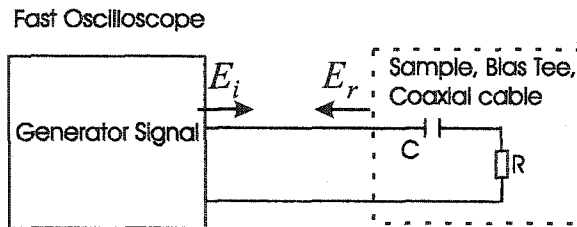


Figure 3.6
Equivalent circuit of the TDR experiment.

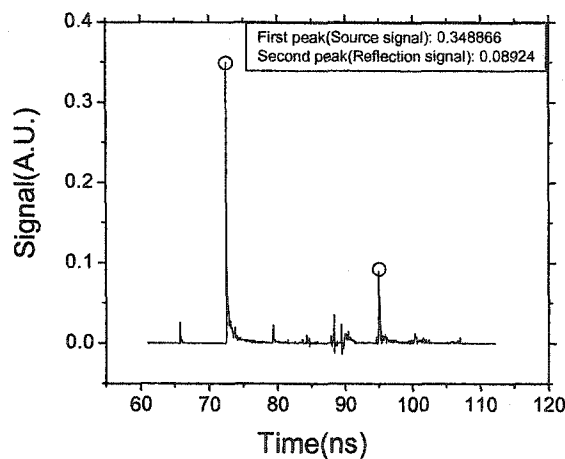


Figure 3.7
Source signal and reflection signal in oscilloscope.

3.3 Experimental setup

Typical sample dimensions are shown in Figure 3.8. A 120 nm-thick gold film was evaporated onto the sample leaving a gap of 330 μm . Samples were mounted on the cold finger of a cryostat which could be pumped down to 4.2×10^{-6} Torr. The experimental setup in Figure 3.9 exhibits how the photoresponse measurement was taken. The two sides of the gold film on the sample were connected to an SMA tab connector (DC-18 GHz) using silver paste or Epoxy paste, which gives the same results. One side of the bias tee was connected to

the SMA tab connector (Picosecond Pulse Labs, Model 5545, 20 GHz) through a coaxial cable, the other side was connected to a cable attached to a 40 GHz digital sampling oscilloscope (Tektronix CSA 803 with a 26 GHz SD-20 sampling head). The bias tee was biased with DC voltage up to 40V. The average system response time was below 50 *ps*, which was limited by trigger jitter, sample geometry, the bandwidth of the bias tee, the coaxial cable and the fast oscilloscope. The cables were covered with aluminum foil for the trigger and the power supply to minimize high frequency external electrical noise.

The amplified Ti:Sapphire laser source produced 100 *fs*, 800 *nm* pulses at a repetition rate of 1.08 KHz. A 10 cm focal length cylindrical lens was used to focus the laser beam down to a 350 *um* × 170 *um* elliptical spot with the major axis parallel to the length of the gap, resulting in a laser intensity up to 52 *mW / cm²* incident onto the gap. A microscope coupled to a CCD camera was used to monitor the beam position on sample. A BBO crystal was used to double the frequency for the excitation wavelength at 400 *nm*. The wave form was taken for positive and negative bias voltages and then subtracted to eliminate spurious baseline effects in the oscilloscope. A noise level down to 0.4 mV was achieved with 128 averages per wave form. In the SCLC experiment configuration (Appendix B), the same sample which had 120 *nm* gold film electrode was connected with an SMA tab connector using silver paste and the SMA tab connector electrodes was attached to a high resistance meter (Model TeraOhm 5 KV, Metrel Com.). Current-voltage data were recorded at several step voltages.

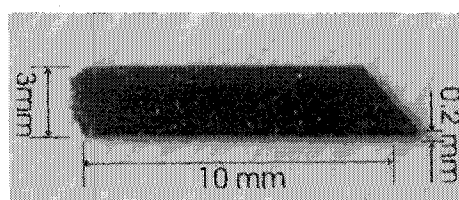


Figure 3.8
Typical dimensions of a TIPS single crystal without gold film. The thickness is 0.2 mm, length is 10 mm and width is 3 mm.

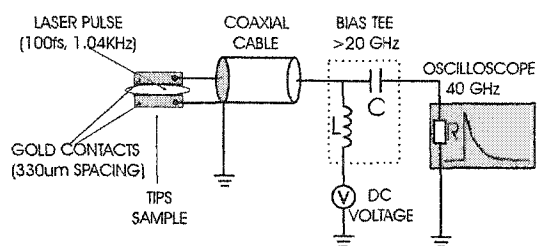


Figure 3.9
Schematic of the setup used for the fast photoresponse experiment. Full or narrow illumination is not indicated. The power supply polarity can be changed.

3.4 Noise reduction

Normally the signal peak is 4-5 mV without amplification, so minimizing the noise from the D.C. power supply, the trigger source for the fast oscilloscope, and other high frequency sources is really critical in our case. All cables and the connection between the cryostat and the bias tee case were covered by aluminum foil to isolate external high frequency (radio frequency) electrical noise. Figure 3.10 represents the noise level after averaging 128 times. Normally the signal peak is 4~5 mV which means that the signal-to-noise ratio (SNR) is 10-12. The spurious base line effect can be eliminated by subtracting the baseline signal when the laser beam is blocked. Figure 3.11 show how the photoresponse wave form was typically taken where the baseline signal effect was subtracted as follows:

$$(\text{photocurrent waveform} + \text{baseline waveform}) - (\text{baseline waveform}) = \text{photocurrent waveform}$$

where the photocurrent waveform+baseline waveform is obtained when the laser illuminates the sample biased with electric field and the baseline waveform is obtained when the laser beam is blocked. However, the baseline waveform will drift with time as shown in Figure 3.12 before noise reduction. In Figure 3.12 the dashed line is the baseline waveform taken at 14:20.

Six minutes later, another baseline waveform is taken. Clearly the baseline waveform shifts with time. In order to minimize the effects of avoid baseline shift upon subtraction of waveform, the wave forms were taken with 128 averages which takes around 110 seconds. The sequences, therefore was to take the laser illumination wave form, then immediately take the beam blocked waveform.

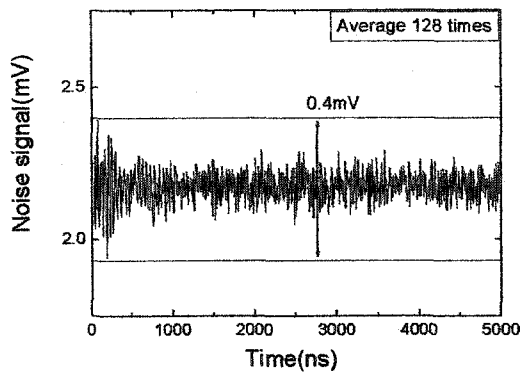


Figure 3.10

Noise level after noise reduction which is averaged 128 times and takes roughly 110 seconds. The noise level is 0.4 mV.

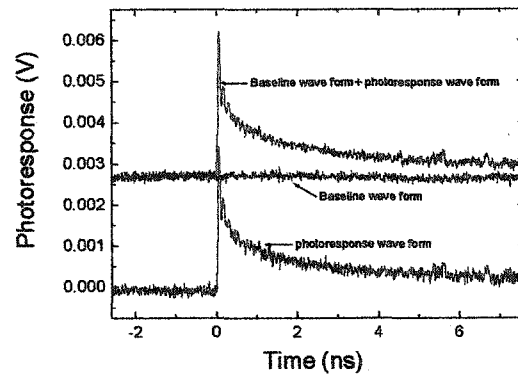


Figure 3.11

A typical fast photoresponse wave form, which was taken by deleting the baseline signal when the laser beam is blocked.

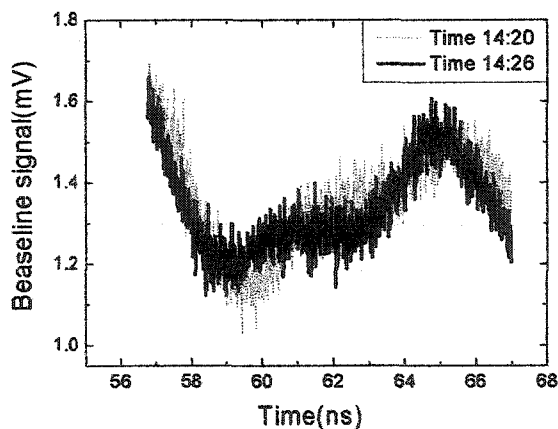


Figure 3.12

The baseline signals at 6 minute intervals, which shows that the baseline shifts over time. The dashed line is the wave form taken at 14:20 and the solid line is the wave form taken at 14:26.

3.5 Laser beam profile

The laser beam profile is needed when we calculate the laser intensity. Due to the laser beam having a Gaussian profile, almost 100% of the laser intensity is contained within $2\omega_0$, where ω_0 is the Gaussian radius. We used a photodiode with a $25 \mu\text{m}$ pinhole to scan the laser beam to get its profile as Figure 3.13 illustrates. Also, we fitted the result to a Gaussian function: $I = I_0 \exp(-\frac{2r^2}{\omega_0^2})$ to get the Gaussian radius and calculate the laser intensity. The x-

axis result was fitted to formula $I = I_{0x} \exp(-\frac{2x^2}{\omega_{0x}^2}) \times I_{0y} \exp(-\frac{2y^2}{\omega_{0y}^2})$ where ω_{0x} and

The laser intensity is the integral $\int_{-\infty}^{+\infty} I_{0x} \exp(-\frac{2x^2}{\omega_{0x}^2}) \times I_{0y} \exp(-\frac{2y^2}{\omega_{0y}^2}) dx dy$ where ω_{0x} and

ω_{0y} are the x-axis and y-axis Gaussian radii respectively. By plugging all values into the following formula, we get the laser intensity.

$$\int_{-\infty}^{+\infty} I_{0x} \exp(-\frac{x^2}{2\omega_x^2}) \times I_{0y} \exp(-\frac{y^2}{2\omega_y^2}) dx dy = P(\infty) = I_{0x} I_{0y} 2\pi\omega_x\omega_y$$

$$= I_{0x} I_{0y} \times 2 \times \pi \times 0.39683\text{mm} \times 0.03822\text{mm}$$

Since $\int_{-\infty}^{+\infty} \exp(-x^2) dx = \sqrt{\pi}$, where $P(\infty)$ is laser power, so laser intensity

$$I_{0x} I_{0y} = \frac{P(\infty)}{2\pi\omega_x\omega_y} = 15\text{mW} / 2 \times \pi \times 0.39683\text{mm} \times 0.03822\text{mm} = 15.7\text{W} / \text{cm}^2$$

when we assume the average laser power is 15 mW.

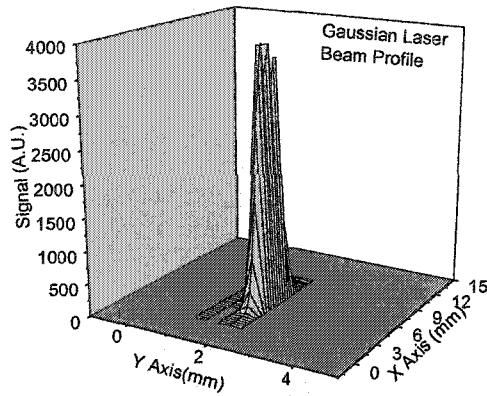


Figure 3.13
Laser beam Gaussian profile which shows that the laser intensity is non-uniform. Average laser power is 15 mW at 800 nm wavelength.

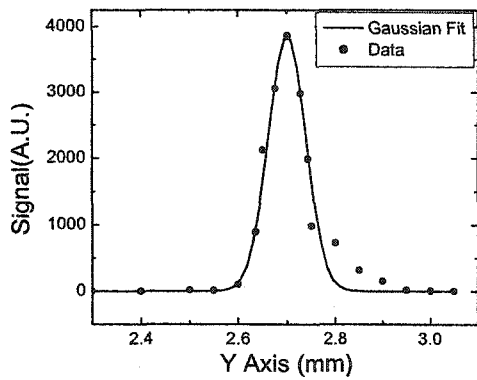


Figure 3.14
X-axis Gaussian beam distribution with Gaussian radius fitted to 0.076 mm.

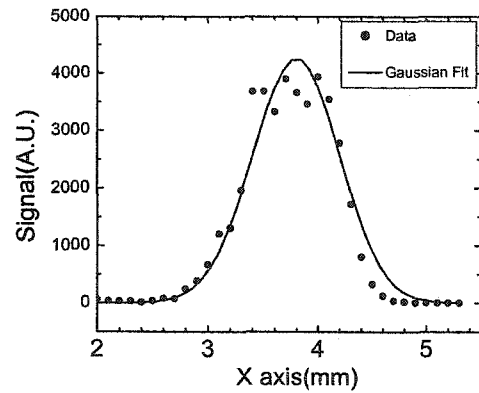


Figure 3.15
Y-axis Gaussian beam distribution with Gaussian radius fitted to 0.79 mm.

Before discussing our results, we consider the following factors which affect interpretation of the transient photoresponse experiments; more details can be found in the Appendices.

a) Illumination region [32, 33, 49]. When the laser beam covers the electrodes, the photoresponse wave form is significantly different from the photoresponse wave form where

the laser spot is focused on the gap center. We interpret this difference due to the non-uniform space charge distribution which produces a space charge field inside the sample.

b) Electric field distribution across the sample [50-56]. Electric field and potential below the sample in the coplanar geometry can be determined with the aid of a sequence of conformal transformation mappings, assuming zero thickness of the electrodes since the electrode thickness is really small compared to the sample [50]. It predicts that the electric field varies gradually below the sample surface [51-53]. TIPS sample thicknesses are between 200-500 μm , which is thick compared to other groups' samples using a similar geometry and micro-stripline switch technique (MSS) [54] in low electric field. We use Montgomery's method [55,56] to calculate the sample effective thickness, employing the known values of the sample's a, b, c directional resistance referred to Anthony group's results [16]. Montgomery's method is pretty useful for calculating the effective thickness using the transformation of a real anisotropic sample with ρ_a, ρ_b, ρ_c and dimensions l'_1, l'_2, l'_3 to an ideal isotropic sample with dimensions l_1, l_2, l_3 since people already know the relationship between isotropic sample dimension and resistivity. Since the space charge limited current (SCLC) voltage-current curves are obtained within $a-b$ plane electrodes, taking the above sample dimensions, the effective thickness of transformation normalized isotropic sample is 0.3193mm for the saturation value $l_3 / (l_1 l_2)^{1/2} = 6.1$. And the ratio between the real effective thickness and the isotropic normalized one is 0.1, so the effective thickness is 32.86 μm which is within one order of the TIPS crystal thickness. More details like SCLC theory, conformal transformation mapping method, and Montgomery's method will be discussed in Appendices B, C and D.

c) System response time (rise time). The rise time is limited by trigger jitter, sample geometry and bandwidth of all coaxial cables, the bias tee and the fast oscilloscope. Promptly after photon excitation, carrier generation, relaxation to a lower energy level, charge carrier recombination, and carrier trapping can all happen within the first few picoseconds. Therefore we expect that the faster the rise time, the more precise the photoresponse measurement will be from which quantum yield, charge carrier mobility, photogeneration mechanics *etc.* can be deduced. In other words, if we can get better response times like 10 ps or less, we can test the photogeneration time limits and get more information about photogeneration and charge carrier transport. In our case, the response time is 50 ps which is comparable to other groups [33, 35]. However from our group's THz experiment result, the photogenerated charge carrier already recombine and fall in traps/defects in this tiny period [28], so what we detected is actually a time-averaged behavior of ultrafast charge carrier photogeneration and transport.

d) Space charge [33, 57, 58]. Immediately after photoexcitation, the initial charge is zero inside the gap since the number of the photoexcited electrons equals the number of photoexcited holes, but an internal field may develop later due to the different diffusion coefficients for electrons and holes as well as charge accumulation near Schottky-type contacts. The non-uniformity of space charge may build up an electric field inside gap in two directions, one is parallel to the electrodes which has nothing to do with photocurrent and the other is perpendicular to gap which has contributions to photocurrent, therefore making the photocurrent smaller and distorting the wave form. Several factors like laser intensity, electric field, and foreign interfacial material at the junction determine the severity of the space charge effect. The total charge can be obtained by integrating the wave form (Appendix E (1)). The typical charge generated is less than 8% of the total charge $Q = CV$, which is stored at the electrodes, where C is the sample capacitance and V is the biased voltage. Therefore the

imbalance between space charges and accumulation charges on the electrodes can be ignored. However, when the laser spot is not uniformly illuminated, even if the amount of space charge is very small compared to the charge accumulated at the electrodes, the space charge field can make the external field smaller, resulting in a different decay. More details about the different behavior between full illumination and narrow illumination will be discussed later.

Chapter 4 Results and discussion

- 4.1 Typical fast photoresponse wave forms
- 4.2 Charge carrier transport and photogeneration in TIPS at room temperature
- 4.3 Charge carrier mobility comparison between SCLC and fast photoresponse experiments
- 4.4 Wave form comparison between full illumination and narrow focus
- 4.5 Electric field and laser fluence dependence
- 4.6 Built-in field at interface

Chapter 4 Results and Discussion

Since the nature of charge carrier photogeneration and transport is a crucial problem in organic crystals, as mentioned earlier in Chapter 2, in this chapter we would like to talk about the interpretation of charge carrier transport and photogeneration mechanisms based on the fast photoresponse wave forms. The charge carrier mobility comparison estimated from the SCLC and fast photoresponse experiments results will be compared. At last, we discuss other concerns like electric field and laser fluence dependence and built-in field effect in our experiment

4.1 Typical fast photoresponse wave forms

In the following sections, we will focus on discussion about recent experiment results such as the charge carrier transport mechanism at room temperature, the charge carrier mobility, photogeneration quantum efficiency, laser fluence dependence, electric field dependence and interface effects. Figure 4.1 is typical photoresponse wave forms at positive electric field and negative electric field at room temperature. Figure 4.2 and 4.3 are typical photoresponse wave forms at different laser fluence and electric field. More detailed discussion about the laser fluence and electric field will be presented in Section 4.5.

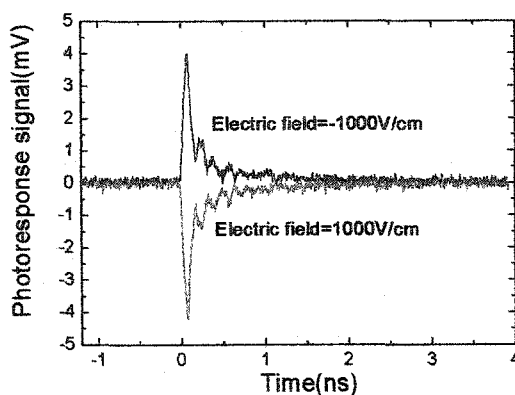


Figure 4.1

Typical photoresponse wave forms at positive electric field and negative electric field at room temperature. The laser power is 5 mW in narrow beam case.

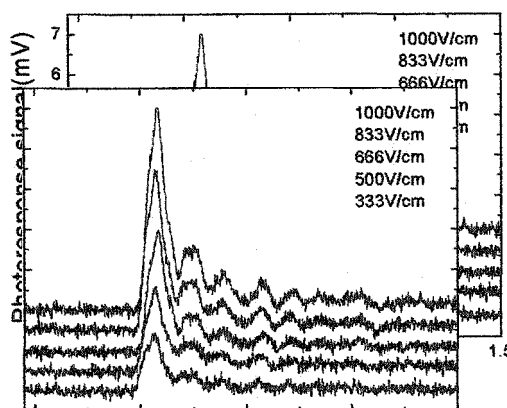


Figure 4.2

Typical photoresponse wave forms at different electric field. The wave forms were shifted up 0.5mV one by one from electric field=333 V/cm. The laser power is 5 mW and kept constant.

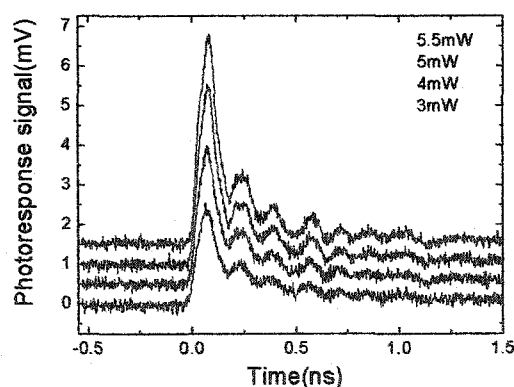


Figure 4.3

Typical photoresponse wave forms at different laser intensity at room temperature. The wave forms were shifted up 0.5 mV one by one from laser power=3 mW. The electric field is 1000 V/cm and kept constant.

4.2 Charge carrier transport and photogeneration in TIPS at room temperature

The only way to clarify which charge carrier transport mechanism is followed, such as the band-like model or the hopping model is to study TIPS crystal photoresponse as a function of

temperature down to low temperature. However, the crystals always cracked at low temperature, (i.e. $T < 200$ K) so the results as shown in Figure 4.6 are not reproducible, but it shows the experimental feasibility in the future. At room temperature, the charge carrier mean free path roughly equal to the lattice constant, so charge carriers are probably localized and they hop site by site. The most successful model [30] to explain such transport in detail is the continuous time random walk (CTRW) model which predicts that the transient photocurrent decays according to a power law, $I(t) \sim t^{-\alpha}$ ($0 < \alpha < 1$). The typical photoresponse wave form of different samples in full illumination case (Figure 4.4) can be fitted to the formula $I(t) \sim t^{-\alpha}$ ($\alpha = 0.5$), which can be interpreted to charge carrier dispersive transport as discussed earlier in Section 1.4.2. The inset in Figure 4.4 is a log-log plot and the solid line has a value 0.5 as a guide to the eye.

At 800 nm excitation wavelength, which is nearby the TIPS crystal absorption edge, fast photocurrent was obtained, which indicates that mobile charge carrier photogeneration is also fast. Meanwhile, the photocurrent peak shows a linear behavior with electric field at 800 nm and 400 nm excitation wavelength and the intercept is zero, which indicates that the primary photoexcitations are mobile charge carriers. If charge carrier photogeneration follows the molecular exciton model, since the exciton binding energy is high (i.e. ~ 0.5 eV), the photocurrent can only happen at high electric fields due to exciton dissociation. In conclusion, in this electric field range, charge carrier photogeneration follows the semiconductor band model.

The rise time in Figure 4.5 suggests that the charge carrier photogeneration is below 50 ps. Hegmann *et al* [28] found of mobile charge carrier in TIPS to be within 1 ps and charge carrier relaxation within 10 ps. However, due to the slow response time of only 50 ps in the photoresponse setup discussed here, the system can not see photogeneration below this time

range. We try to correlate the rise time in terms of a capacitance $C = \epsilon\epsilon_0 \frac{A}{d}$ (A is electrode area and d electrode spacing). Table 4.1 lists different sample dimensions and photoresponse rise times. But it's not obvious to see any relation between sample dimensions and rise time as shown in Appendix E (2). Since the rise time is larger than circuit constant time RC , we attribute the large values to contact resistance of the sample and silver/Epoxy paste, as well as other stray impedance in the sample mount.

Table 4.1 Sample Dimensions and Corresponding Photoresponse Rise Time

Sample	d (mm)	L (mm)	W (mm)	Measurement rise time (ps)
#10	0.2	3.7878	1.25	36
#12	0.2	2.8875	1.29	46
#13	0.2	4.4	1.25	66
#14	0.2	4.35	1.53-1.51	40
#15	0.2	2.5	1.25-1.20	44.5
#16	0.2	1	1	57.5

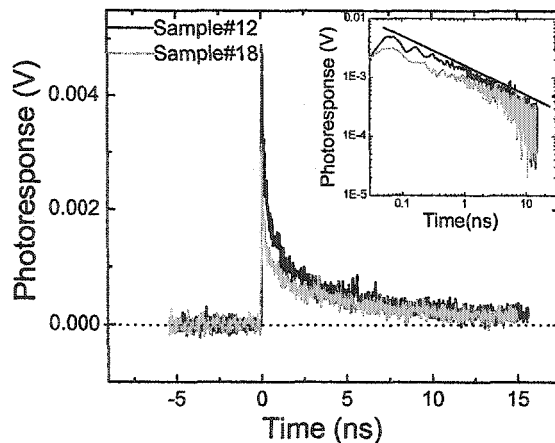


Figure 4.4

Different sample wave forms which fit power-law decay formula $I(t) \sim t^{-\alpha}$ indicates dispersive transport behavior. Inset is a log-log plot which shows power-law decay. The straight line shows power=-0.5.

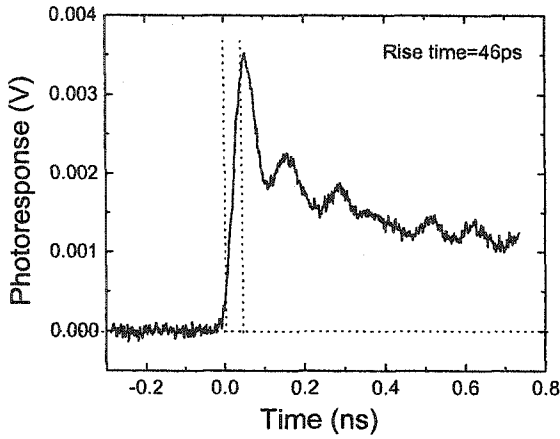


Figure 4.5
Photoresponse wave form shows system rise time of 46 ps which has no relation with sample dimensions.

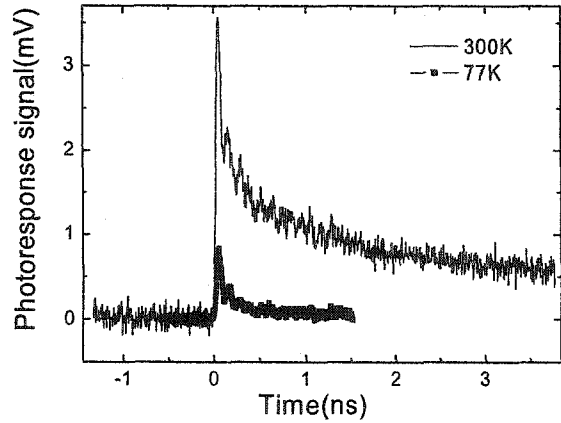


Figure 4.6
Photoresponse wave forms at 300 K and 77 K. The laser power and electric field are same in both cases.

4.3 Charge carrier mobility comparison between SCLC and fast photoresponse experiments

Normally, the mobility of organic molecular crystals at room temperature is less than $1 \text{ cm}^2 / \text{Vs}$. In order to compare the charge carrier mobility results obtained from transient experiments, the space charge limited current (SCLC) current-voltage curve in Figure 4.7 was fit to $I \sim V^2$ to calculate mobility using the formula [59]

$$I_{SCLC} = \frac{9\epsilon\epsilon_0\mu V^2}{8L^3} \dots\dots\dots 4.1$$

where I_{SCLC} is the current in the trap-free regime, μ is the mobility, V is the applied voltage across the electrode spacing L , and ϵ is the dielectric constant of the sample. From the graph $\frac{9\epsilon\epsilon_0\mu}{8L^3} = 0.0027 \text{ nA} / \text{V}^2$ and using literature value $\epsilon = 3$, we can obtain the mobility

$$\mu = 0.05 \text{ cm}^2 / \text{Vs}.$$

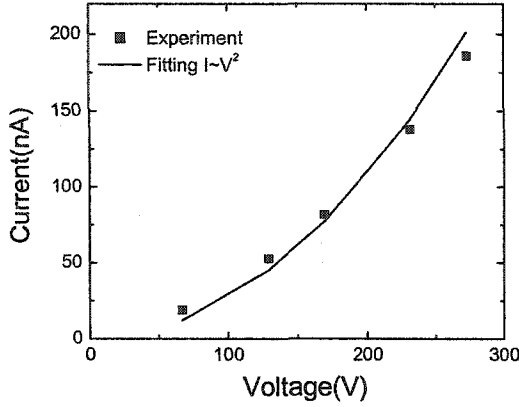


Figure 4.7

SCLC result which is fitted to equation 4.1 to deduce mobility value. The solid line is a fit to the data with the power set to 2 by purpose. The power-law that best fits the data is actually $I \sim V^{1.8}$.

Also the mobility can be deduced from [34]

$$I_p = N_{ph} \eta e E \mu / L \dots\dots\dots 4.2$$

in fast photoresponse experiment, where I_p is the photocurrent peak, N_{ph} is the number of absorbed photons, η is the quantum efficiency and L is the electrode spacing (330 μm). Assuming unity quantum yield, minimum mobility $\mu = 1.6 \times 10^{-4} \text{ cm}^2 / Vs$ can be obtained at 1000 V/cm at 800 nm and 400 nm excitation wavelength. (Mobility calculation in Appendix E (3) and Appendix E (4))

However, compared to the SCLC, the calculated mobility result from the fast photoresponse wave form is only one percent of that of the SCLC if we use the above formula. We attribute the significant discrepancy to two reasons: (1) recombination of carriers within the 50 ps system response time and (2) effective electric field thickness.

The terahertz time domain spectroscopy result on a TIPS single crystal (Figure 4.9) which has sub-picosecond rise time shows that at room temperature the photocurrent peak decays to approximately 3%~5% of its initial value at 50 ps due to charge carrier recombination and traps [28]. The THz experiment excitation wavelength and temperature are the same as ours,

thus, except for the system detection response time, all parameters are the same. In other words, the photogeneration and charge carrier transport are the same processes in both cases. Also the quantum efficiency is the same in both experiments according to modified Onsager model discussed in Section 2.2.2 because of the very low electric field assuming this model applies. Therefore the same decay in fast photoresponse experiment was expected in our experiment. In summary the wave form during 50 ps system response time range is average behavior of charge carrier photogeneration and transport and the photocurrent peak value will decay to 5% of initial value at 50 ps. Also, even assuming that all photons are absorbed and the electric field penetration is much less than sample thickness, only part of the photogenerated charge carriers can feel the full electric field. Taking all factors into account since 20 times is due to system response time, 5 times is due to cable attenuation as discussed in section 3.2 and 10 times is due to electric field effective thickness as discussed in Appendix D, we can get the mobility $\mu = 1.6 \times 10^{-4} \times 20 \times 5 \times 10 = 0.16 \text{ cm}^2 / Vs$ which is consistent with the SCLC experiment and other groups' results [43]. It is worthy to note that in this case we assume the quantum efficiency is 100%. However since quantum efficiency is less than unity, the real mobility should be larger than $\mu = 0.16 \text{ cm}^2 / Vs$. If the quantum efficiency is around 10%, then $\mu = 1.6 \text{ cm}^2 / Vs$ should be obtained at room temperature. The calculated mobility at room temperature is comparable to other results reported in functionalized pentacene [28] and pentacene using different techniques [60-62]. However, the mobility improvement is limited by weak molecule interaction and chemical and physical impurities. Jurchescu *et al.* [43] used vacuum sublimation technique to get ultra-pure pentacene crystals with nobilities as high as $\mu = 35 \text{ cm}^2 / Vs$ at room temperature.

The quantum efficiency can be calculated from

$$\eta = \frac{\int idt}{N_{photons}} \dots\dots\dots 4.3$$

where $N_{photons}$ is the total number of the absorbed photons and $\int idt$ is the total generated charges which can be obtained from the wave form integration. This calculation is based on the assumption that all photogenerated charge carriers are collected by the electrodes which is not ease in our sample geometry. Also, taking the system response time into account, the quantum efficiency 1.74×10^{-7} and was obtained at 800 nm and 400 nm excitation wavelength respectively. (Charge charier photogeneration quantum efficiency calculation is in Appendix E (5) which refers to Figure 4.8 a and 4.8 b)

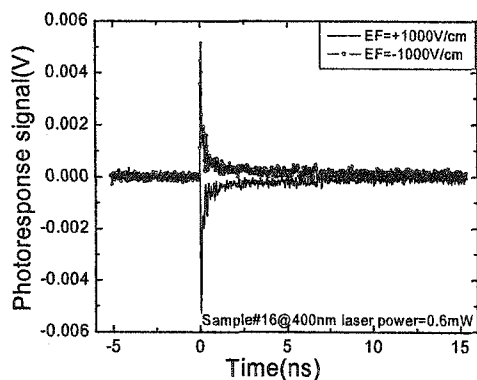


Figure 4.8 (a)
Fast photoresponse wave form at 800 nm excitation wavelength to calculate charge carrier mobility. The electric field are ± 1000 V/cm and laser power is 6 mW.

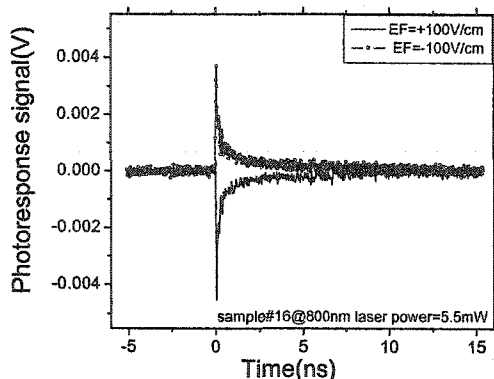


Figure 4.8 (b)
Fast photoresponse wave form at 400 nm excitation wavelength to calculate charge carrier mobility. The electric field is ± 1000 V/cm and laser power is 5.5 mW.

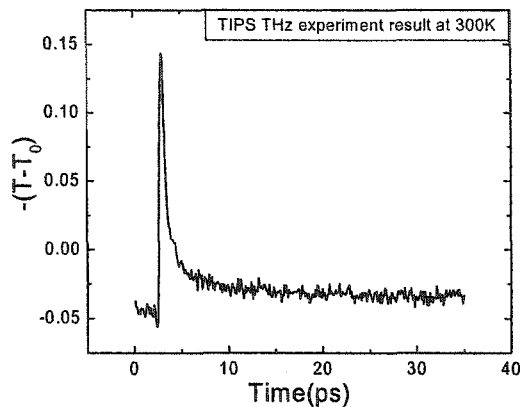


Figure 4.9
THz result which shows system response time and photocurrent decay to 5% at 35 ps (Adapted from O. Ostroverkhova's result)

4.4 Wave form comparison between full illumination and narrow focus

Figure 4.10 and Figure 4.11 show that at same excitation laser power, the wave forms are totally different. Since absorption spectrum of different crystals in solvent are the same, the different decay behavior which maybe due to chemical difference can be eliminated. We attribute this different behavior due to the following reasons: 1) space charge effect and 2) large traps/defects density. At full illumination, the charge carriers, which are generated in the illumination area, keep neutrality since the amounts of holes and electrons are equal if we assume that trap density is the same everywhere. From the full illumination wave form, we estimate the typical charge imbalance to be less than 8% of the total charges, which is stored at the electrodes, therefore this effect can be ignored (Appendix E(1)). In summary in the full illumination case, the space charge amount is small and the build-up field is small. However, when the laser beam is focused to a line narrower than the electrode spacing, the cloud of photoexcited electrons and holes move apart by the action of the external field. At the inner region of the illumination, charge carriers keep neutrality, but at the outer region a space charge field builds up due to the traps and the Gaussian beam property that most of the laser intensity is within the Gaussian radius. The space charge field weakens the external field and

there is almost no field forcing force charge carriers to drift. Therefore, the photocurrent decays faster. Another reason for the different decay behavior is the large trap/defect density. In the full illumination case, part of charge carriers fill up all traps or defects and part of them still drift to the electrodes. On the other hand in the narrow laser beam case, all charge carriers after photoexcitation fill up traps/defects, which results in fast decay behavior.

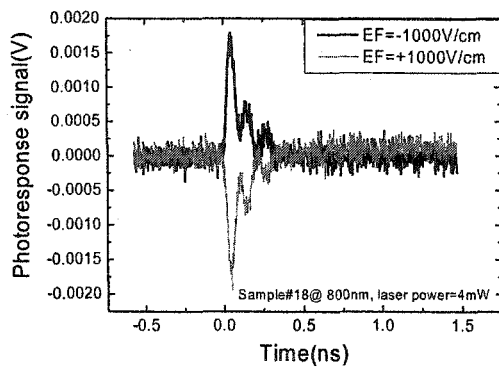


Figure 4.10

Photoreponse wave form at narrow laser beam illumination. The laser power is 4 mW and electric field is ± 1000 V/cm. The sample is same as the full illumination case.

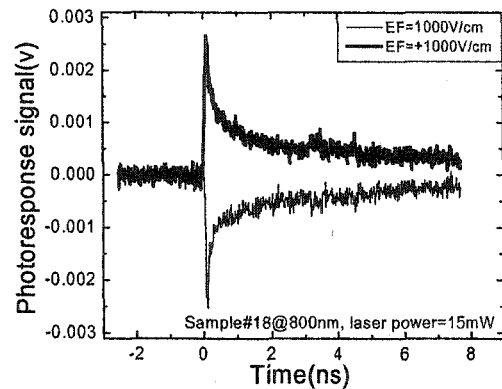


Figure 4.11

Photoreponse wave form at full illumination. The laser power is 15 mW and electric field is ± 1000 V/cm.

4.5 Electric field and laser fluence dependence

Ideally, charge carrier photogeneration and transport mechanisms can be studied by measuring the dependence of photoreponse as a function of different photoexcited wavelengths, temperature, light intensity and electric field. We found that the photocurrent peak is proportional to the applied field at 400 nm and 800 nm excitation wavelengths up to 1200 V/cm (Figure 4.12). The photocurrent peak as a function of laser intensity has a super-linear dependence at 800 nm and a linear dependence at 400 nm (Figure 4.13). Also, the

normalized wave forms are independent of light intensity and electric field in the explored range (Figure 4.14).

The charge carrier photogeneration is independent of electric field. However our electric field is only up to 1200 V/cm which is quite small, and any effect like exciton dissociation due to electric field is not obvious. We might also expect lower photoresponse peak at higher electric field due to the phonon interaction discussed in Chapter 2.

The super-linear dependence in the intensity dependence can be due to a mixture of two-photon and one-photon excitations. Silver *et al.* [63] found that the photocurrent increases as the square of the light intensity in anthracene, and Hasegawa and Kepler reported that photon carriers can be produced in anthracene crystal by the interaction between singlet excitons [30]. The rate of the increase of charge carrier is given by

$$\frac{dn}{dt} = \beta N^2 - \gamma n^2 \dots\dots\dots 4.4$$

where n is the density of charge carriers, β and γ are singlet-singlet interaction and recombination constants and N is the density of singlet excitons. If we assume that singlet excitons are produced by two-photon absorption, the density N is $N = KF^2$ where F is the laser intensity and K is a constant. By inserting N to the above equation then integrating one obtains the total number of carriers n_t produced in the crystal during the laser duration Δt :

$$n_t = (\beta / \gamma)^{1/2} KF^2 \tanh[(\beta\gamma)^{1/2} \Delta t KF^{1/2}] \dots\dots\dots 4.5$$

If the condition is in the high laser intensity which means the argument of hyperbolic tangent is larger than 1.5,

$$n_i \approx (\beta/\gamma)^{1/2} KF^2 \propto F^2 \dots\dots\dots 4.6$$

So n_i is proportional to the square of laser the intensity. In our case, we get the power between 1.4-1.6, so the photogeneration is probably a mixture of two-photon and one-photon excitations or excited-state absorption.

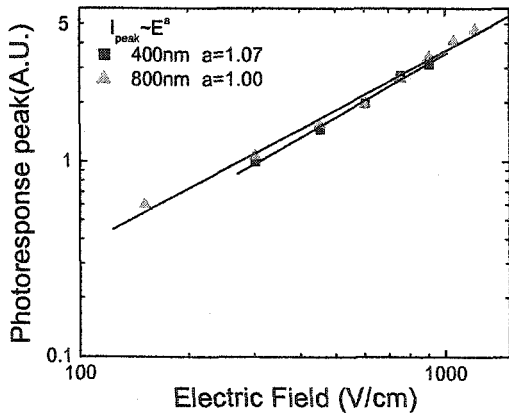


Figure 4.12
Photocurrent peak vs. electric field at 800 nm and 400 nm excitation wavelength in room temperature when the laser beam is full illumination.

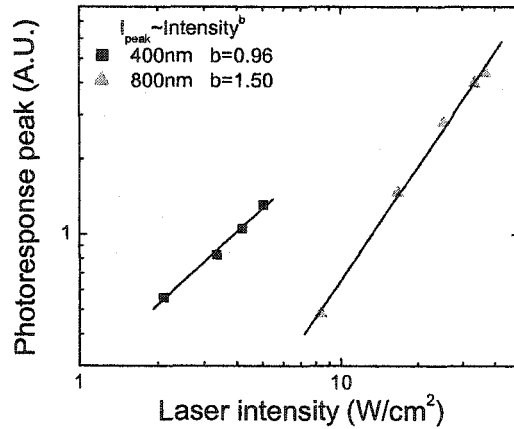


Figure 4.13
Photocurrent peak vs laser fluence at 800 nm and 400 nm excitation wavelength in room temperature when the laser beam is full illumination.

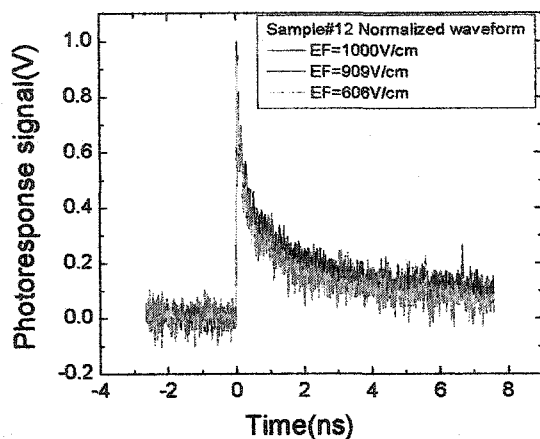


Figure 4.14

Normalized photoresponse waveform at different electric fields when the laser power is 15 mW and kept constant. It shows that wave forms have no difference at different electric fields.

4.6 Built-in field at interface

Figure 4.15 shows the zero electric field photoresponse peaks at different positions when the laser beam was focused down to $150\ \mu\text{m}$ and made to scan the sample surface including the crystal and the gold film. The positions were marked as position 1, 2, 3, etc. in the schematic scan setup diagram (Figure 4.16), as indicated by the arrows. The laser beam position was monitored by the CCD camera coupled to the microscope.

At zero electric field, the photoresponse signal has significant peaks at both sides of the junctions but is zero at the center (Figure 4.17), which indicates the existence of a built-in field at the TIPS/Au junction. When the excitation energy is larger than the barrier height between metal and organic crystal, electrons from the gold film can be injected into the crystal. We eliminate this photoinjection effect since the photoresponse signal is really small when the laser illuminates the gold film compared to when the laser illuminates the interface at zero field. Compared to the photocurrent peak biased with positive and negative fields, it indicates that the direction of the built-in field is from the TIPS to Au and the field amplitude is comparable to the external field as illustrated in Figure 4.18 (a), (b) and (c). Again, the fast decay behavior proves that focusing the laser beam can produce space charge effects which

weaken built-in fields and charge carriers fall into traps very fast. At positions 2 and -2, symmetrical peaks were not expected because laser beam was illuminated at tiny different regions on both sides of the interface which microscope cannot tell. The built-in field exists at the TIPS/Au is not surprising and other groups reported potential barrier at Pentacene/Al and Pentacene/n-Si [64-66]. In fact, the barrier height can be accurately determined by photoconductivity measurements. However the fast photoresponse already gives clues about junction behavior which implies charge carrier transport mechanics [33, 67]. It shines light on exploration of carrier dynamics at junction utilizing fast photoresponse.

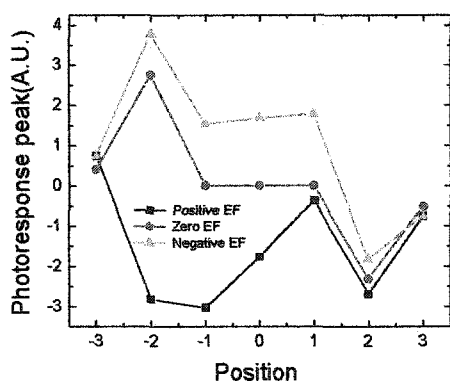


Figure 4.15
Photoresponse peaks at different positions at positive, negative and zero biased electric fields.

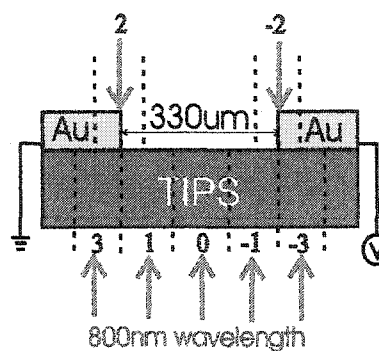


Figure 4.16
Scan geometry to see interface effect. The below arrows are clearly to tell different illumination regions.

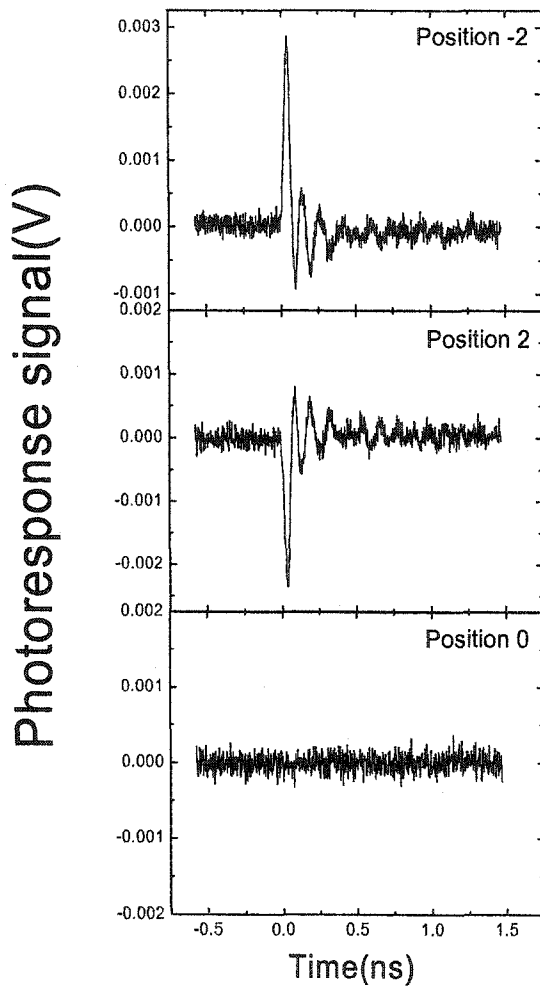


Figure 4.17
Photoresponse wave form at different positions biased with zero electric field. The laser power is 2.88 mW in narrow beam case.

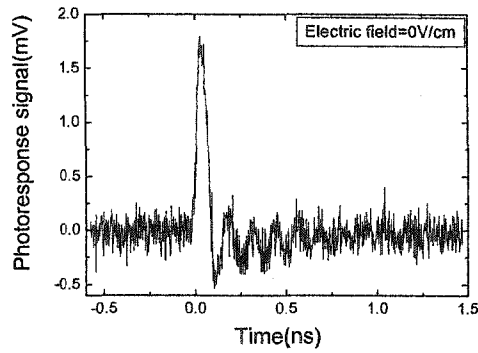


Figure 4.18 (a)
Interface photoresponse wave forms biased with zero electric field at room temperature. The laser power is 2.88 mW in narrow beam case.

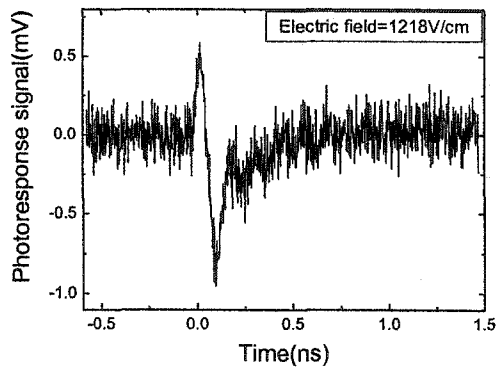


Figure 4.18 (b)
Interface photoresponse wave forms biased with negative electric field at room temperature. The laser power is 2.88 mW in narrow beam case.

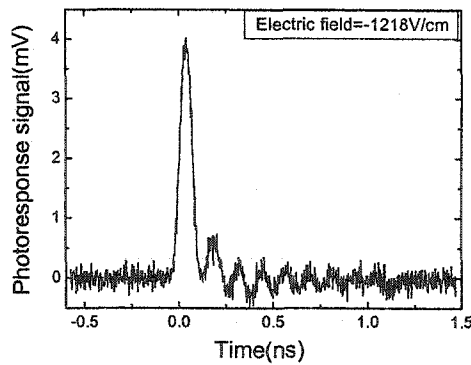


Figure 4.18 (c)
Interface photoresponse wave forms biased with positive electric field at room temperature. The laser power is 2.88 mW in narrow beam case.

Chapter 5 Conclusion and future work

In summary, we used a coplanar electrode geometry and a fast sampling oscilloscope with system response time below 50 ps to observe fast photoresponse of functionalized pentacene single crystals. The main motivation is to clarify the controversy about charge carrier photogeneration and transport mechanism in these kinds of crystals. The photoresponse wave form exhibited a power-law decay $t^{-\alpha}$ ($\alpha \approx 0.5$), which indicates the charge carrier transport is dispersive. The charge carrier mobility $\mu \approx 0.1 \text{ cm}^2 / \text{Vs}$ was obtained after we considered the system response time and the electric field effective thickness, which is a typical problem in transient experiments that employ co-planar electrodes geometry. The photocurrent peak is proportional to electric field at 400 nm and 800 nm excitation wavelengths, which does not show molecular exciton dissociation mechanism due to the low electric fields. Meanwhile, the photoresponse at 800 nm excitation wavelength indicates that the primary photoexcitation are mobile charge carriers and follows the semiconductor band model. Also photocurrent peak shows a linear relation with laser fluence at 400 nm and a super-linear relation at 800 nm, which may indicate that one-photon and two-photon excitation process involved respectively. Since we evaporated gold film onto the functionalized pentacene as electrodes, the interface effect can be observed in our case. The interface photoresponse indicates that a built-in field exists at the TIPS/Au junction and is directed from the TIPS to Au.

Although a fast photoresponse of the TIPS at room temperature was observed and the electric-field and fluence dependence were studied, a conclusive answer for the nature of the charge carrier photogeneration and transport mechanism in organic molecular crystal cannot be found. The charge carrier photogeneration mechanism can be clarified by exploring the photoresponse at different excitation wavelengths and higher electric fields. Furthermore the

charge carrier transport, which is either hopping or band-like transport, can be clarified by low temperature and higher electric field experiments. When we tried to figure out the discrepancy between the mobility results obtained from the SCLC with that of fast photoresponse experiment, the electric field effective thickness should be considered since the sample thickness can not be neglected. Using conformal transformation method, an electric field computer simulation can be done to exactly know the effective thickness of the electric field. Because organic electronics are based on organic thin film and metal film contacts, it is very important to investigate the charge carrier transport in ordered and amorphous TIPS thin films and junctions between organic film and metal, therefore the interface of TIPS/Au is concerned in our experiment. Even though we observed the interesting photoresponse behaviors at TIPS/Au interface which shows that these experiments make it feasible to investigate organic/metal junctions, the detailed behaviors of such as charge carrier transport, barrier height and the majority carrier in TIPS (P or N type), *etc* need to be known in the future.

Appendix

Appendix A (1) Crystallographic Data on Polyacenes [Adapted from Ref. 30.]

Table A (1)

<i>Crystallographic Data on Polyacenes</i>					
Parameters	Naphthalene	Anthracene	Tetracene	Pentacene	TIPS
Crystal structure	Monoclinic	Monoclinic	Triclinic	Triclinic	Triclinic
Space group	$P2_1/a$	$P2_1/a$	$P\bar{1}$	$P\bar{1}$	$P\bar{1}$
a (Å)	8.24	8.56	7.90	7.90	7.5650
b (Å)	6.00	6.04	6.03	6.06	7.75
c (Å)	8.66	11.16	13.53	16.01	16.835
α $^\circ$	90.0	90.0	100.3	101.9	89.15
β $^\circ$	122.9	124.7	113.2	112.6	92.713
γ $^\circ$	90.0	90.0	86.3	85.8	83.63
V (Å) ³	360	474	583	692	960.9
Z	2	2	2	2	1
d_{cal}	1.17	1.24	1.29	1.33	*
d_{exp}	1.15	1.25	1.29	1.32	*
M (daltons)	128.19	178.24	228.3	278.36	*

V: Unit cell volume in (Å)³; Z: Number of molecules in unit cell
d: Density of the crystal; d_{exp} : Experimental results; d_{cal} : Calculation results
M: Molecular weight(in daltons)

Appendix A (2) Ionization Potentials, Electron Affinities, Predicted Band Gaps of Polyacenes [Adapted from Ref. 30.]

Table A (2)

<i>Ionization Potentials, Electron Affinities, Predicted Band Gaps</i>						
Compound	I_g (eV)	A_g (eV)	I_c (eV)	E_C^a (eV)	E_g^b (eV)	ε_g (eV)
Benzene	9.24	-0.95	*	*	*	*
Naphthalene	8.15	-0.2	6.76	5.4	5.6	5.2
Anthracene	7.47	0.58	5.70	3.9	3.3	3.9
Naphthacene	7.04	0.88	5.28	3.5	2.6	3.0
Pentacene	6.74	1.2	4.85	3.0	1.8	*

$E_C = 2I_c - I_g$; $\varepsilon_g = 2I_c - I_g - A_g$
 I_c : Ionization energy of crystal; I_g : Ionization energy of free molecule
 A_g : Free molecule affinity; ε_g : Band gap *: no data so far

Appendix B

Space-charge-limited Current [34]

In order to compare the charge carrier mobility results obtained from transient experiments with space-charge-limited current experiments, the same sample attached to the SMA connector was used to get current-voltage curve. The current transport through the sample is governed by the concentration of charge carriers injected from the contacts. Consider the I-V plot in Figure B (1) of an insulator sandwiched between two metallic electrodes. At low voltage there is negligible injection of carrier from electrode; the thermal equilibrium density of charge carrier in the absence of voltage is greater than the density injected through the contacts, therefore the current obeys Ohm's law. When this condition is not fulfilled, the current become space charge limited: the organic material between the electrodes is no longer neutral, excess charges have been injected. These charges develop a potential that influences the I-V characteristics. The space charge generated by injection of charges has two components: the mobile charge carrier and eventually the filled traps. The filling of traps by injected charge carrier gives electrically charged centers, which may contribute to the formation of the space charge. First consider the trap-free case: all injected electrons or holes remain free in the conduction band. The current may be estimated form the time t required for the charge to go from one electrode to the other:

$$I_{SCLC} = \frac{Q}{t_t} \dots\dots\dots B (1)$$

where I_{SCLC} is the space charge limited current and t_t is the transit time for the charge carriers. The transit time t_t may be expressed in terms of the carrier mobility μ and the field

$$E = \frac{V}{d} \text{ in the material where } d \text{ is the spacing of electrodes.}$$

$$t_t = \frac{d^2}{\mu V} \dots\dots\dots B (2)$$

The two electrodes form a capacitor whose capacitance may be approximated by $C = \epsilon\epsilon_0 \frac{A}{d}$ where ϵ is the dielectric constant for the organic material. If a charge Q is present in the organic insulator, the corresponding voltage may be expressed as $Q=CV$.

So the space charge limited current can be obtained from the formulas:

$$I_{SCLC} = \frac{9}{8} \epsilon\epsilon_0 \mu \frac{AV^2}{d^3} \dots\dots\dots B (3)$$

When a material contains shallow traps, the space charge is not only composed of the mobile carrier, but also of the trapped charges. The residence time inside the traps is lower than the transit time because trapped charges are readily freed thermally. Under these condition, the above formula is still applicable, provided the mobility is replace by an effective mobility. $\mu_{eff} = \theta\mu$, therefore the current is still proportional to the square of the applied voltage. When deep traps are considered, the previous approximation cannot be made. The residence time of the charges in the traps becomes longer than the transit time, thus the space charge limited current depends on the density of traps and on their distribution inside the band gap.

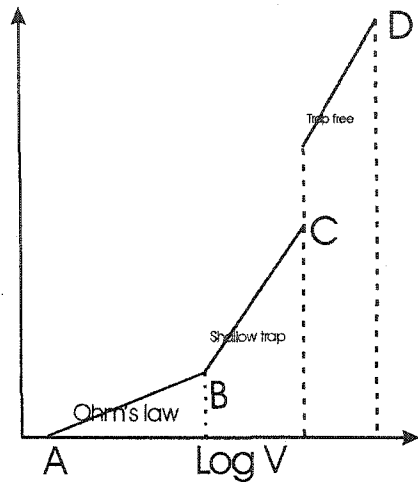


Figure B (1)

Current-voltage plot of a typical insulator, which includes Ohm's law region, shallow defects and deep defects region.

Appendix C

Electric field distribution using conformal transformation mapping method [45]

Based on the condition that the thickness of the electrodes were assumed to be zero, the conformal transformation mapping method yields an evaluation of the potential and flux distribution in terms of the coordinates of the transformed geometry if all equi-potential surfaces and electric field lines are normal or parallel to the surface of dielectric distribution.

In the transformed geometry, the equipotential surface is represented by planes parallel to the u axis, with the conducting element represented by the plane $v = 1$. Potential is measured along the v -axis from zero to unity. The lower case letters in Figure C (1) and C (2) indicate that the corresponding points in two geometries. It must be pointed out that if u and v are the real and imaginary parts of an analytic function w and if one (in this case v) is selected to represent the potential, the other determines the flux crossing a simple curve according to the expression:

$$\Psi_{0a} = -\varepsilon[u(a) - u(0)] \dots\dots\dots C (1)$$

where 0 and a the two end points of the curve.

The left and right planes of Figure C (1) are mirror images of each other as are the upper and lower half planes. Thus, evaluation in only one quadrant is sufficient. Since the v_2 axis provides a portion of the quadrant boundary, the value of u on this axis defines the flux emanating from the conductor in this quadrant, i.e., taking $u(a) = 0$,

$$\Psi_{0a} = \varepsilon_1 u(0) \dots\dots\dots C (2)$$

and the total flux between the conductor and the grounded planes is

$$\Psi = 2u(0)(\varepsilon_1 + \varepsilon_2) \dots\dots\dots C (3)$$

The total charge q on the conductor is Ψ , so the capacitance between the conductor and grounded planes is

$$C = \frac{q}{\Phi} = 2u(0)(\varepsilon_1 + \varepsilon_2) \dots\dots\dots C (4)$$

with the potential difference Φ equal to unity. The capacitance between two adjacent electrodes is one fourth this value since above equation represents the capacitance for two parallel gaps and the potential difference Φ between the two alternately charged electrodes is twice that used in C(4).

We will evaluate the impedance for the structure in Figure C (1). To begin with, consider the case $\varepsilon_1 = \varepsilon_2$. If the dielectric in the whole section is uniform and lossless, the TEM mode can be propagated along the structure with the characteristic impedance $Z = \sqrt{\mu\varepsilon} / C$.

Substituting C (4) into C (5), we can get $Z = \sqrt{\frac{\mu}{\varepsilon}} \frac{1}{4u(0)}$. When $\varepsilon_1 \neq \varepsilon_2$,

$$\text{the } Z = \frac{1}{4u(0)} \sqrt{\frac{2\varepsilon_0}{\varepsilon_1 + \varepsilon_2}}.$$

The problem of determining the electrostatic field around parallel coplanar strip lines of zero thickness is really a two-dimensional one. Let a denote half the width of each element

and b half the distance between the axes of any two adjacent elements. The following transformation sequences will change the complex potential plane to simple one.

$$v = \frac{b}{\pi}(\lambda - \pi) \dots\dots\dots C (6)$$

$$\lambda = i \ln \frac{\zeta^2 - 1 + 2l\zeta}{\zeta^2 - 1 - 2l\zeta} \dots\dots\dots C (7)$$

$$\zeta = \sqrt{k} \sin\left[\frac{2K}{\pi} \sin^{-1} kz\right] \dots\dots\dots C (8)$$

$$z = \frac{1}{k} \cos\left[\frac{\pi}{4} \frac{K'}{K} \frac{W}{\Phi}\right] \dots\dots\dots C (9)$$

where

$$l = \cot \frac{a\pi}{2b}, k = \tan^2 \frac{a\pi}{4b}, K = K(k) = \int_0^{\pi/2} \frac{d\phi}{\sqrt{1 - k^2 \sin^2 \phi}}, K' = K(k'), k' = \sqrt{1 - k^2} \text{ and } \Phi \text{ is the}$$

voltage of the enclosed strip line.

To determine the electric field pattern in the region between the two lines $v_1 = \pm b$, it is necessary to invert each equation of the sequences given above. Straightforward inversion of (5) and (6) yields the following formulas:

$$\lambda_1 = \frac{\pi}{b}(v_1 + b) \dots\dots\dots C (10)$$

$$\lambda_2 = \frac{\pi}{b}v_2 \dots\dots\dots C (11)$$

and

$$\zeta_1 = \frac{1}{\sqrt{2}} [(\Lambda_1^2 + \Lambda_2^2)^{1/2} + \Lambda_1]^{1/2} - l \frac{\sinh \lambda_2}{\cosh \lambda_2 - \cos \lambda_1} \dots\dots\dots C (12)$$

$$\zeta_2 = -\frac{1}{\sqrt{2}} [(\Lambda_1^2 + \Lambda_2^2)^{1/2} - \Lambda_1]^{1/2} - l \frac{\sin \lambda_1}{\cosh \lambda_2 - \cos \lambda_1} \dots\dots\dots C (13)$$

where

$$\Lambda_1 = 1 - I^2 \frac{\sin^2 \lambda_1 - \sinh^2 \lambda_2}{(\cosh \lambda_2 - \cos \lambda_1)^2} \dots\dots\dots C (14)$$

$$\Lambda_2 = I^2 \frac{2 \sin \lambda_1 \sinh \lambda_2}{(\cosh \lambda_2 - \cos \lambda_1)^2} \dots\dots\dots C (15)$$

while the inversion of (8) and (9) yields

$$u = \frac{2\Phi}{K} F(\alpha, k), \quad v = \frac{2\Phi}{K'} F(\beta, k') \dots\dots\dots C (16)$$

where $F(\phi, k)$ is the elliptic integral of the first kind, and

$$\sin \alpha = \left[\frac{k}{4\zeta_1^2} \left(1 + \frac{\zeta_1^2}{k} + \frac{\zeta_2^2}{k} - \sqrt{A} \right) \cdot \left(\frac{1}{k_2} + \frac{\zeta_1^2}{k} + \frac{\zeta_2^2}{k} - \sqrt{B} \right) \right] \dots\dots\dots C (17)$$

$$\sin \beta = \left[\frac{k}{4\zeta_2^2} \left(1 - \frac{\zeta_1^2}{k} - \frac{\zeta_2^2}{k} - \sqrt{A} \right) \cdot \left(\frac{1}{k_2} - \frac{\zeta_1^2}{k} - \frac{\zeta_2^2}{k} - \sqrt{B} \right) \right] \dots\dots\dots C (18)$$

with

$$A = \left(1 - \frac{\zeta_1^2}{k} + \frac{\zeta_2^2}{k} \right) + \left(2 \frac{\zeta_1 \zeta_2}{k} \right)^2 \dots\dots\dots C (19)$$

$$B = \left(\frac{1}{k^2} - \frac{\zeta_1^2}{k} + \frac{\zeta_2^2}{k} \right)^2 + \left(2 \frac{\zeta_1 \zeta_2}{k} \right)^2 \dots\dots\dots C (20)$$

In summary, the potential and flux distribution is

$$u = \frac{2\Phi}{K} F(\alpha, k), \quad v = \frac{2\Phi}{K'} F(\beta, k'), \quad \text{where the parameters are indicated in above discussion.}$$

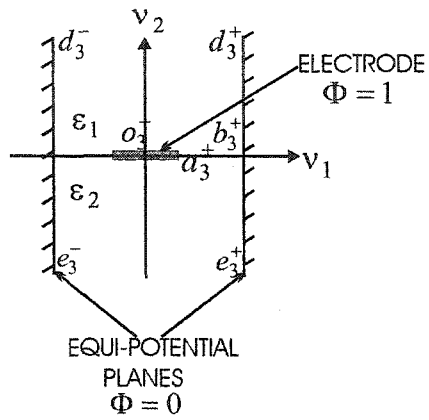


Figure C (1)

Electrode structure shows a single electrode bounded by equipotential planes. The boundary is indicated by the lower case characters, which are corresponded to Figure C(2).

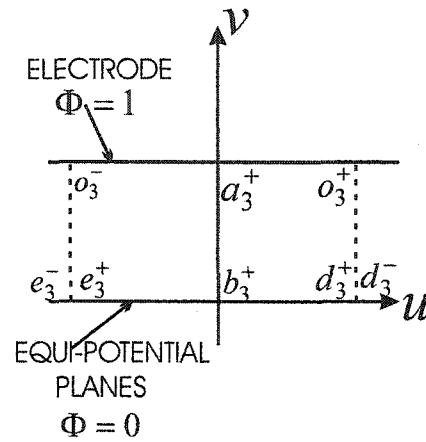


Figure C (2)

Transformed parallel planes with the corresponding image points indicated by the same lower case letters.

Table C (1) Boundary Condition of Original Potential Planes and Conformed Transformation Planes

	v_1	v_2	u	v
d^+	b	+	$\frac{1}{2}k_1\pi$	0
e^+	b	-	$\frac{3}{2}k_1\pi$	0
b^+	b	0	0	0
a^+	a	0	0	Φ
0^+	0	+0	$\frac{1}{2}k_1\pi$	Φ
0^-	0	-0	$\frac{3}{2}k_1\pi$	Φ
a^-	-a	0	$k_1\pi$	Φ
b^-	-b	0	$k_1\pi$	0
e^-	-b	-	$\frac{1}{2}k_1\pi$	0
d^-	-b	+	$\frac{3}{2}k_1\pi$	0

Appendix D Sample calculation of electric field effective thickness

People already calculated the voltage-current relations for a rectangular prism of isotropic material, with dimensions l_1, l_2, l_3 and resistivity ρ . The sample anisotropic resistivity can be change to equivalent isotropic one using a simple transformation. [51]

Suppose that a rectangular sample has been cut from an anisotropic material with dimensions l'_1, l'_2, l'_3 and with corresponding ρ_1, ρ_2, ρ_3 respectively. From Wasscher's relation this will map to an equivalent solid of dimension l_1, l_2, l_3 and resistivity ρ , where

$$l_i = l'_i(\rho_i / \rho)^{1/2} \dots\dots\dots D (1)$$

$$\rho = (\rho_1\rho_2\rho_3)^{1/3} \dots\dots\dots D (2)$$

If the observed voltage-current ratios are R_1 when the voltage probes aligned in the l'_1 direction and R_2 for the l'_2 direction, these same voltage-current ratios would by definition be observed on the equivalent isotropic sample in the l_1 and l_2 directions, respectively. In isotropic sample the formula

$$\rho = H E R_1 \dots\dots\dots D (3)$$

is valid where H is a function of l_2 / l_1 as shown in Figure D (1). In the above formula E is effective thickness, which is equal to the actual thickness l_3 when $l_3 \ll (l_1 l_2)^{1/2}$. In normalized form, $E / (l_1 l_2)^{1/2}$ depends mainly on $l_3 / (l_1 l_2)^{1/2}$ and is nearly independent of l_2 / l_1 over much of its useful range.

For the case of a thin sample $l_3 \ll (l_1 l_2)^{1/2}$, from (2) we can get

$$(\rho_2 / \rho_1)^{1/2} = (l_2 / l_1) \times (l'_1 / l'_2) \dots\dots\dots D (4)$$

and it is easily shown that

$$(\rho_1 \rho_2)^{1/2} = H l_3 R_1 \dots\dots\dots D (5)$$

From (4) and (5), ρ_1 and ρ_2 are easily calculated. If ρ_3 is known to be same as ρ_1 or ρ_2 , the determination is complete.

If sample thickness must be taken into account, and if ρ_3 is equal to either ρ_1 or ρ_2 , the procedure is a little different as following. For illustration it will be assumed that $\rho_3 = \rho_1$.

After using (4) to determine ρ_1 / ρ_2 , calculate

$$l_3 / (l_1 l_2)^{1/2} = (\rho_1 / \rho_2)^{1/4} \times l'_3 / (l'_1 l'_2)^{1/2} \dots\dots\dots D (6)$$

From Figure D (2) we obtain $E / (l_1 l_2)^{1/2}$ corresponding to $l_3 / (l_1 l_2)^{1/2}$. If one calculate

$$E' / (l'_1 l'_2)^{1/2} = (\rho_2 / \rho_1)^{1/4} \times E / (l_1 l_2)^{1/2} \dots\dots\dots D (7)$$

Then $(\rho_1 \rho_2)^{1/2}$ can be calculated from (5) using E' in place of l'_2 .

In cases where ρ_3 is not equal to ρ_1 or ρ_2 and the sample thickness must be taken into account, (6) and (7) become

$$l_3 / (l_1 l_2)^{1/2} = \rho_3^{1/2} / (\rho_1 \rho_2)^{1/4} \times l'_3 / (l'_1 l'_2)^{1/2} \dots\dots\dots D (8)$$

$$E' / (l'_1 l'_2)^{1/2} = (\rho_2 \rho_1)^{1/4} / \rho_3^{1/2} \times E / (l_1 l_2)^{1/2} \dots\dots\dots D (9)$$

There is no straightforward procedure for determining the ρ 's in this case, but it appears that one could assume a value for ρ_3 , carry out the measurements, and calculations for two perpendicular sample faces, then modify ρ_3 until a self-consistent result was obtained for the three ρ 's.

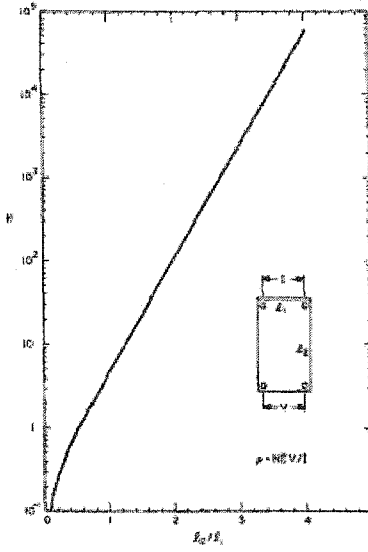


Figure D (1)
H parameter dependence on l_2 / l_1 in isotropic material.

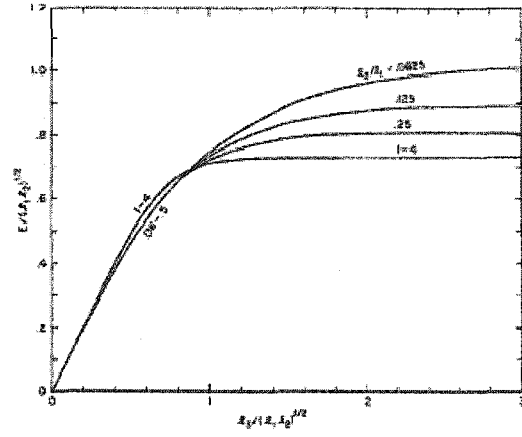


Figure D (2)
Normalized effective thickness dependence on normalized thickness in isotropic material.

If the sample dimensions are $l_1' = 3\text{mm}$, $l_2' = 0.33\text{mm}$, $l_3' = 0.2\text{mm}$; and $\rho_1 = 2.6 \times 10^6 \Omega\text{cm}$, $\rho_2 = 4.7 \times 10^8 \Omega\text{cm}$, $\rho_3 = 3.2 \times 10^{10} \Omega\text{cm}$, which are referred from Anthony *et al* data, the transformation dimensions is

$$l_1 = l_1' (\rho_1 / \rho)^{1/2} = 3\text{mm} \times (2.6 \times 10^6 \Omega\text{cm} / 3.39422 \times 10^8 \Omega\text{cm})^{1/2} = 0.388323\text{mm}$$

$$l_2 = l_2' (\rho_2 / \rho)^{1/2} = 0.33\text{mm} \times (4.7 \times 10^8 \Omega\text{cm} / 3.39422 \times 10^8 \Omega\text{cm})^{1/2} = 0.262566\text{mm}$$

$$l_3 = l_3' (\rho_3 / \rho)^{1/2} = 0.5\text{mm} \times (3.2 \times 10^{10} \Omega\text{cm} / 3.39422 \times 10^8 \Omega\text{cm})^{1/2} = 1.94193\text{mm}$$

where

$$\rho = (\rho_1 \rho_2 \rho_3)^{1/3} = (2.6 \times 10^6 \Omega\text{cm} \times 4.7 \times 10^8 \Omega\text{cm} \times 3.2 \times 10^{10} \Omega\text{cm})^{1/3} = 3.39422 \times 10^8 \Omega\text{cm}$$

Therefore the ratio between the real effective thickness and the transformation effective thickness is

$$E'/(l_1' l_2')^{1/2} = (\rho_2 \rho_1)^{1/4} / \rho^{1/2} \times E/(l_1 l_2)^{1/2} \Rightarrow \frac{E'}{E} = \frac{(\rho_1 \rho_2)^{1/4} (l_1' l_2')^{1/2}}{\rho_3^{1/2} (l_1 l_2)^{1/2}}$$

$$= \frac{(4.7 \times 10^8 \Omega cm \times 2.6 \times 10^6 \Omega cm)^{1/4} (3mm \times 0.33mm)^{1/2}}{(3.2 \times 10^{10} \Omega cm)^{1/2} (0.388323mm \times 0.262566mm)^{1/2}} = 0.1029$$

According Figure D (2), if we select the saturation value=1, we can get the maximum value for the transformation effective thickness.

$$E/(l_1 l_2)^{1/2} = 1 \Rightarrow E = (0.388323mm \times 0.262566mm)^{1/2} = 0.3193124mm$$

So the maximum real effective thickness is

$$\frac{E'}{E} = 0.1029 \Rightarrow 0.1029 \times 0.3193124mm = 0.032857mm = 32.857\mu m$$

Also if we select sample dimensions $l_1' = 0.33mm$, $l_2' = 3mm$, $l_3' = 0.2mm$; we still get the same results.

Appendix E

Appendix E (1) The space charge effect in full illumination case

After photogeneration charge carrier generated in sample will build up field inside gap between two electrodes due to the electrons and holes different drift velocities, thus the external field will be affected. The number of the charges accumulated at electrode is $Q_{electrode} = CV$ where C is sample capacitance and V is the applied voltage.

$Q_{electrode} = CV = 4.827273 \times 10^{-14} \times 40 = 1.93091 \times 10^{-12} \text{ Coulomb}$, where $C = 4.827273 \times 10^{-2} \text{ pF}$, $V = 40 \text{ Volt}$ in our case.

The total charge generated after laser illumination is the wave form integration area $\int idt$.

$\int idt = 8.11 \times 10^{-3} \times 10^{-9} / 50 = 1.622 \times 10^{-13} \text{ Coulomb}$, thus the ratio between the charges accumulated at electrode and the space charge is

$0.1622 / 1.9309 = 0.084 \sim 8\%$ which indicates the space charge effect can be neglected.

Appendix E (2) Sample capacitance calculation

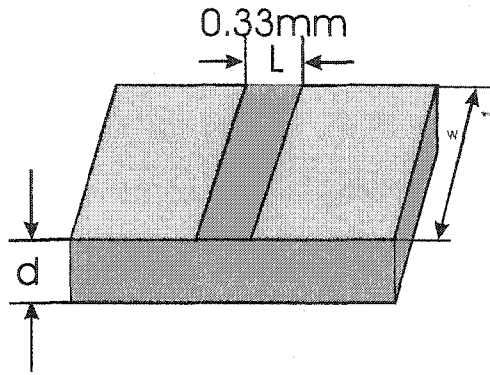


Figure E (1)
Sample dimensions.

The sample capacitance can be calculated from the following formula $C = \frac{\epsilon\epsilon_0 A}{L}$

where ϵ is the dielectric constant, A is the electrode area and L is the electrodes spacing.

Then

$$\begin{aligned} C &= \frac{\epsilon\epsilon_0 A}{L} = \frac{3 \times 8.85 \times 10^{-14} \text{ F/cm} \times 0.3 \text{ cm} \times 0.02 \text{ cm}}{0.033 \text{ cm}} \\ &= 4.8 \times 10^{-14} \text{ F} = 4.8 \times 10^{-2} \text{ pF} \end{aligned}$$

This calculation is smaller than real case since effective electrical field thickness is smaller than sample thickness. The capacitance of other parts in the circuit is negligible compared to the sample capacitance, so the circuit time constant $RC = 4.8 \times 10^{-2} \text{ pF} \times 50 \Omega = 2.4 \text{ ps}$ when we assume the impedance is 50Ω . This calculation result is smaller than the real system response time 50 ps . The difference may due to the higher contact resistance, which is larger than 50Ω . Therefore the rise time is determined by the contact proprieties and it has no relation with the sample dimensions.

Appendix E (3) Mobility calculation from SCLC experiment result

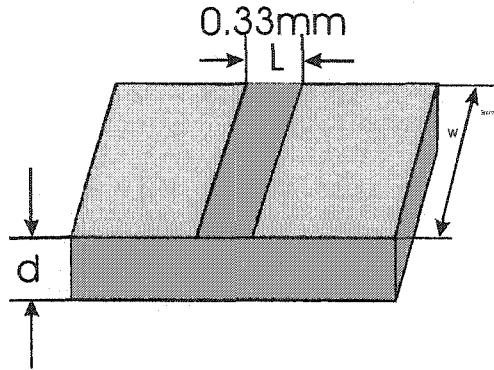


Figure E (1)
Sample dimensions.

From SCLC experiment we can calculate the charge carrier mobility using the following

formula $I_{SCLC} = \frac{9}{8} \epsilon \epsilon_0 \mu \frac{AV^2}{L^3}$ where μ is the charge carrier mobility, A is the electrode area, ϵ is the sample dielectric constant, L is the electrode spacing and V is the across voltage.

As illustrated in the above sample dimensions $L=0.33\text{mm}$, $d=0.2\text{mm}$, $w=3\text{mm}$, and the fitting value from SCLC curve $I/V^2 = 2.7 \times 10^{-12}$, we can get:

$$\frac{I}{V^2} = 2.7 \times 10^{-12} = \frac{9}{8} \epsilon \epsilon_0 \mu \frac{wd}{L^3},$$

$$2.7 \times 10^{-12} = \frac{9}{8} \times 3 \times 8.5 \times 10^{-14} (F/cm) \mu \frac{0.3\text{cm} \times 0.02\text{cm}}{(0.033\text{cm})^3}$$

$$\text{So } \mu = 0.05\text{cm}^2 / \text{Vs}$$

If we take into account the shallow trap as discussed in Appendix B, the real value should be larger than this result.

Appendix E (4) Mobility calculation from fast photoresponse experiment

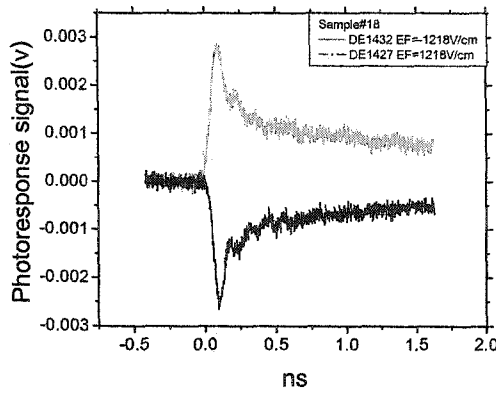


Figure E (2)

Fast photoresponse wave form at 800nm excitation wavelength.

The charge carrier mobility can be deduced from the following formula,

$$I_p = N_{ph} \eta e E \mu / L$$

where I_p is the fast photoresponse peak, N_{ph} is the number of absorbed photons, η is the quantum efficiency and L is the electrode spacing.

From the fast photoresponse wave form, it shows that $I_p = V / R = 2.7 \times 10^{-3} V / 50 \Omega = 5.4 \times 10^{-5} A$ when the laser pulse frequency is 1.04 KHz and laser excitation wavelength is at 800nm (1.55eV), so the total photon number is

$$N = \frac{\text{laserpower}}{h\nu \times \text{frequency}} = \frac{15 \times 10^{-3} W}{1.55 eV \times 1.6 \times 10^{-19} \text{ Coulomb} \times 1040 \text{ Hz}} = 5.82 \times 10^{13}$$

$$\text{Then } \mu = \frac{I_p L}{N_{ph} \eta e E} = \frac{5.4 \times 10^{-5} A \times 0.033 \text{ cm}}{5.81575 \times 10^{13} \times 1.6 \times 10^{-19} \text{ Coulomb} \times 1218 V / \text{cm}} = 1.6 \times 10^{-4} \text{ cm}^2 / \text{Vs}$$

Clearly this calculated mobility is much smaller than that of the SCLC experiment result.

Appendix E (5) Quantum efficiency calculation from fast photoresponse result

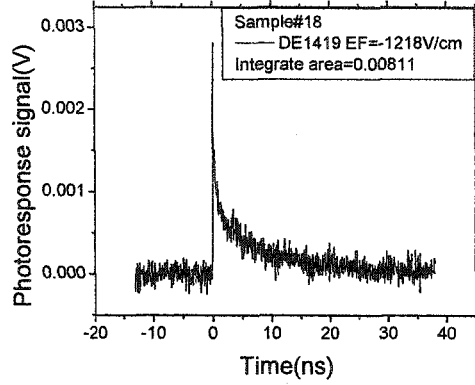


Figure E (3)
Fast photoresponse wave form at
800nm excitation wavelength.

The quantum efficiency can be calculated from the following formula

$$\eta = \frac{\int idt}{eN_{\text{photon}}}, \text{ where } N_{\text{photons}} \text{ is the total absorbed photons and } \int idt \text{ is the total charges}$$

generated which can be obtained from wave form integration. The total photon number is

$$N = \frac{\text{laserpower}}{h\nu \times \text{frequency}} = \frac{15 \times 10^{-3} \text{ W}}{1.55 \text{ eV} \times 1.6 \times 10^{-19} \text{ Coulomb} \times 1040 \text{ Hz}} = 5.82 \times 10^{13}$$

where the laser power is 15mW and laser pulse frequency is 1.04 KHz. From the fast photoresponse wave form integration result $\int idt = 8.11 \times 10^{-3} \times 10^{-9} \text{ V} / 50 \Omega = 1.6 \times 10^{-13} \text{ Coulomb}$

So the quantum efficiency

$$\eta = \frac{\int idt}{eN_{\text{photon}}} = \frac{1.6 \times 10^{-13} \text{ Coulomb}}{1.6 \times 10^{-19} \text{ Coulomb} \times 5.82 \times 10^{13}} = 1.7 \times 10^{-7}.$$

However, taking into account system response time and effective electric field, the reasonable result can be obtained.

References

- [1] W. Warta, N. Karl, *Phys. Rev. B*, 32, 1172(1985)
- [2] L. B. Schein, A. R. McGhie, *Phys. Rev. B*, 20, 1631(1979)
- [3] L. B. Schein, R. W. Anderson, R. C. Enck, *J. Chem. Phys.* 71, 3189(1979)
- [4] J. H. Schön, C. Kloc, *Appl. Phys. Lett.*, 78, 3821(2001)
- [5] R. W. I. de Boer, T. M. Klapwijk, A. F. Morpurgo, *Appl. Phys. Lett.*, 83, 4345(2003)
- [6] W. A. Schoonveld, J. Wildeman, D. Fichou, P. A. Bobbert, B. J. van Wees, T. M. Klapwijk, *Nature*, 404, (2000)
- [7] R. J. Hamers, *Nature*, 412, (2001)
- [8] D. J. Gundlach, T. N. Jackson, D. G. Schlom, S. F. Nelson, *Appl. Phys. Lett.*, 74, 3302(1999)
- [9] D. Knipp, R. A. Street, A. Volkel, J. Ho, *J. Appl. Phys.*, 93, 347(2003)
- [10] C. D. Dimitrakopoulos, P.R.L. Malenfant, *Adv. Mater.* 14, 99 (2002)
- [11] A. Hepp, H. Heil, W. Weise, M. Ahles, R. Schmechel, H. von Seggern, *Phys. Rev. Lett.*, 91, 157406-1(2003)
- [12] E. A. Silinsh, V. Capek, *Organic Molecular Crystals: Interaction, Localization, and Transport Phenomena*, (New York, American Institute of Physics, 1994)
- [13] M. Fox, *Optical Properties of Solids*, (Oxford University Press, 2001)
- [14] R. C. Haddon, X. Chi, M. E. Itkis, *J. Phys. Chem. B* 106, 8288 (2002)
- [15] The data was downloaded from the results of Oregon Medical Laser Center, <http://omlc.ogi.edu/spectra/PhotochemCAD/html/anthracene.html>
- [16] J. S. Brooks, D. L. Eaton, J. E. Anthony, S. R. Parkin, *Curr. Appl. Phys.* 1, 301(2001)
- [17] T. Tokumoto, J. S. Brooks, R. Clinite, X. Wei, *J. Appl. Phys.*, 92, 5208(2002)
- [18] J. E. Anthony, D. L. Eaton, S. R. Parkin, *Org. Lett.*, 4, 15(2002)
- [19] J. Cornil, J. Ph. Callbert, J. L. Bredas, *J. Am. Chem. Soc.* 123, 1250(2001)

- [20] A. G. Markelz, A. Roitberg, E. Heilweil, *J. Chem. Phys. Lett.*, 320, 42(2000)
- [21] M. Walther, B. Fisher, M. Schall, H. Helm, *Chem. Phys. Lett.*, 77, 2452(2000)
- [22] M. Brucherseifer, M. Nagel, P. H. Bolivar, H. Kurz, A. Buttner, *Appl. Phys. Lett.*, 77, 4049(2000)
- [23] P. U. Jepsen, W. Schairer, I. H. Libon, U. Lemmer, N. E. Hecker, *Appl. Phys. Lett.*, 79, 1291(2001)
- [24] M. C. Nuss, D. H. Auston, F. Capasso, *Phys. Rev. Lett.*, 58, 2355(1987)
- [25] R. Huber, F. Tauser, A. Brodschelm, M. Bichler, G. Abstreiter, *Nature*, 414, 286(2001)
- [26] M. C. Beard, G. M. Turner, C. A. Schmuttenmaer, *J. Appl. Phys.*, 90, 5915(2001)
- [27] V. K. Thorsmølle, R. D. Averitt, X. Chi, D. J. Hilton, D. L. Smith, A. P. Ramirez, A. J. Taylor, *Appl. Phys. Lett.*, 84, 891(2004)
- [28] F. A. Hegmann, R. R. Tykwinski, K.P.H. Lui, J. E. Bullock, J. E. Anthony, *Phys. Rev. Lett.* 89, 227403 (2002)
- [29] R. G. Kepler, *Phys. Rev.* 119, 1226(1960)
- [30] J. Mort, D. M. Pai, *Photoconductivity and Related Phenomena* (Elsevier, Amsterdam, 1976)
- [31] W. Warta, R. Stehle, N. Karl, *Appl. Phys. A*, 36, 163(1985)
- [32] D.H. Auston, *IEEE J. Quantum Electronics* QE-19, 4, 639 (1983)
- [33] D. Moses, *Philos. Mag. B*, Vol 66, No. 1, 1(1992)
- [34] C. H. Lee, G. Yu, D. Moses, *Phys. Rev. B* 48, 15425(1993)
- [35] S. D. Phillips, A. J. Heeger, *Phys. Rev. B* 38, 6211(1988)
- [36] M. Pope, C. E. Swenberg, *Electron Processes in Organic Crystals* (World Scientific, Singapore, 1997)
- [37] K.C. Kao, W. Hwang, *Electrical Transport in Solids*, (Pergamon press, 1981)

- [38] N.S. Sariciftic, Primary Photoexcitation in Conjugated Polymer: Molecular Exciton versus Semiconductor Band Model (World Scientific, Singapore, 1997)
- [39] W. Warta, S. Stehle, N. Karl, Physical Review B, 1172(1985)
- [40] L. B. Schein, A. R. McGhie, Physical Review B, 20, 1693(1979)
- [41] A. Szymanski, M. M. Labes, J. Chem. Phys. 50, 1898(1969)
- [42] R. W. I. de Boer, M. Jochemen, T. M. Klapwijk, A. F. Morpurgo, J. Niemax, A. K. Tripathi, J. Pflaum, arXic:cond-mat/0308391.V2(2003)
- [43] O. D. Jurchescu, J. Baas, Thomas T. M. Palstra, Appl. Phys. Lett., 84, 3061(2004)
- [44] V. K. Thorsmolle, R. D. Averitt, X. Chi, D. J. Hilton, D. L. Smith, A. P. Ramirez, A. J. Taylor, Appl. Phys. Lett. 84, 891(2004)
- [45] S. F. Nelson, Y. Y. Lin, D. J. Gundlach, T. N. Jackson, Appl. Phys. Lett. 72, 1854(1998)
- [46] E. H. Roderick, R. H. Williams, Metal-Semiconductors Contacts, (Oxford Scientific Publications, 1987)
- [47] "Time Domain Reflectometry Theory", Hewlett-Packard Application Note 1304-2, 1998
- [48] "Evaluating Microstrip with Time Domain Reflectometry", Hewlett-Packard Application Note 1304-1, 1998
- [49] C.H. Lee, Picosecond Photoelectric Devices, (Academic press, New York, 1984)
- [50] Y. C. Lim, R. A. Moore, IEEE Trans. on electron devices, ED-15, 3, 173 (1968)
- [51] J. D. Wasscher, Philips. Res. Repts, 16, 187(1961)
- [52] J. B.D. Soole, H. Schumacher, IEEE Journal of quantum electronics, 3, 737 (1991)
- [53] P. J. Sellin, M. B.H. Breese, IEEE Trans. on nuclear science, 6, 2307(2001)
- [54] D. Moses, M. Sinclair, A. J. Hegger, Phys. Rev. Lett. 58, 2710(1987)
- [55] M. Sinclair, D. Moses, A. J. Hegger, Solid St. Commun. 59, 343(1986)

- [56] H. C. Montgomery, J. Appl. Phys. 42, 2971(1971)
- [57] N. E. Fisher, D. J. Willock, J. Phys.:Condens. Matter, 4, 2517(1992)
- [58] D. Moses, Phys. Rev. B 53, 4462(1996)
- [59] M. A. Lampert, P. Mark, Current Injection in Solids, (Academic Press Inc., New York, 1970)
- [60] S. F. Nelson, Y. Y. Lin, D. J. Gundlach, T. N. Jackson, Appl. Phys. Lett., 72, 1854(1998)
- [61] Y. S. Yang, S. H. Kim, J. Lee, H. Y. Chu, L. Do, H. Lee, J. Oh, T. Zyung, Appl. Phys. Lett., 80, 1595(2002)
- [62] V. Y. Butko, X. Chi, D. V. Lang, A. P. Ramirez, Appl. Phys. Lett., 83, 4773, (2003)
- [63] M. Silver, D. Olness, M. Swicord, R.C. Jarnagin, Phys. Rev. Lett. 10, 12(1963)
- [64] Kahn A, Koch N, Gao W Y, J. Polym Sci. Pol. Phys. 41, 2529 (2003)
- [65] S. S. Kim, Y. S. Choi, Kibum Kim, Appl. Phys. Lett. 82, 639 (2003)
- [66] J. Lee, D. K. Hwang, C.H. Park, Thin solid film, in press, (2003)
- [67] Sze. S. M. Physics of Semiconductor Devices (Wiely, New York, 1981)